

















NuSTAR observations of a varying-flux quasar in the Epoch of Reionization

LEA MARCOTULLI ^{1,2,*} THOMAS CONNOR ^{3,4} EDUARDO BAÑADOS ⁵ PETER G. BOORMAN ⁶ GIULIA MIGLIORI ⁷
BRIAN W. GREFFENSTETTE ⁶ EMMANUEL MOMJIAN ⁸ ANETA SIEMIGINOWSKA ³ DANIEL STERN ⁴
SILVIA BELLADITTA ^{5,9} C. C. CHEUNG ¹⁰ ANDREW FABIAN ¹¹ YANA KHUSANOVA ⁵ CHIARA MAZZUCHELLI ¹²
SOFÍA ROJAS-RUIZ ¹³ AND C. MEGAN URRY ^{1,2}

¹*Yale Center for Astronomy & Astrophysics, 52 Hillhouse Avenue, New Haven, CT 06511, USA*

²*Department of Physics, Yale University, P.O. Box 208120, New Haven, CT 06520, USA*

³*Center for Astrophysics | Harvard & Smithsonian, 60 Garden St., Cambridge, MA 02138, USA*

⁴*Jet Propulsion Laboratory, California Institute of Technology, 4800 Oak Grove Drive, Pasadena, CA 91109, USA*

⁵*Max-Planck-Institut für Astronomie, Königstuhl 17, D-69117 Heidelberg, Germany*

⁶*Cahill Center for Astrophysics, California Institute of Technology, 1216 East California Boulevard, Pasadena, CA 91125, USA*

⁷*INAF Istituto di Radioastronomia, via Gobetti 101, 40129 Bologna, Italy*

⁸*National Radio Astronomy Observatory, P.O. Box O, Socorro, NM 87801, USA*

⁹*INAF-Osservatorio di Astrofisica e Scienza dello Spazio di Bologna, Via Piero Gobetti 93/3, 40129 Bologna, Italy*

¹⁰*Space Science Division, Naval Research Laboratory, Washington, DC 20375, USA*

¹¹*Institute of Astronomy, Madingley Road, Cambridge, CB3 0HA, UK*

¹²*Instituto de Estudios Astrofísicos, Facultad de Ingeniería y Ciencias, Universidad Diego Portales, Avenida Ejército Libertador 441, Santiago, Chile.*

¹³*Department of Physics and Astronomy, University of California, Los Angeles, CA, 90095*

ABSTRACT

With enough X-ray flux to be detected in a 160 s scan by *SRG/eROSITA*, the $z = 6.19$ quasar CFHQS J142952+544717 is, by far, the most luminous X-ray source known at $z > 6$. We present deep (245 ks) *NuSTAR* observations of this source; with ~ 180 net counts in the combined observations, CFHQS J142952+544717 is the most distant object ever observed by the observatory. Fortuitously, this source was independently observed by *Chandra* ~ 110 days earlier, enabling the identification of two nearby ($30''$ and $45''$ away), fainter X-ray sources. We jointly fit both *Chandra* and *NuSTAR* observations—self-consistently including interloper sources—and find that, to greater than 90% confidence, the observed 3 – 7 keV flux varied by a factor of ~ 2.6 during that period, corresponding to approximately two weeks in the quasar rest-frame. This brightening is one the most extreme instances of statistically significant X-ray variability seen in the Epoch of Reionization. We discuss possible scenarios that could produce such rapid change, including X-ray emission from jets too faint at radio frequencies to be observed.

Keywords: Quasars (1319) — Radio loud quasars (1349) — X-ray astronomy (1810) — X-ray quasars (1821) — Time domain astronomy (2109)

1. INTRODUCTION

One of the more exciting revelations of the early Universe has been the discovery of supermassive black holes (SMBHs) with masses in excess of $10^9 M_{\odot}$ well into the first billion years after the Big Bang ($z \gtrsim 6$; Fan et al. 2023). Such masses are comparable to the upper reaches of mass found at lower redshift (e.g., Shen et al. 2011), implying that

these black holes have already reached maturity despite their young age. This insight raises a critical question, however, of what mechanism produced these black holes originally (Volonteri et al. 2021). Seeding hypotheses can generally be classified into either light seeds ($M_{\text{BH}} \lesssim 10^2 M_{\odot}$, e.g., Bromm et al. 1999; Whalen & Fryer 2012) or heavy seeds ($M_{\text{BH}} \gtrsim 10^4 M_{\odot}$, e.g., Lodato & Natarajan 2006; Wise et al. 2019); the latter tend to require more complex and fine-tuned models to produce (Habouzit et al. 2016; Luo et al. 2020), but the former can only generate the observed SMBHs with faster-than-Eddington growth (Wang et al. 2021a). As such, the current path toward understanding these first SMBHs lies

Corresponding author: Lea Marcotulli, Thomas Connor
lea.marcotulli@yale.edu, thomas.connor@cfa.harvard.edu

* NHFP Einstein Fellow

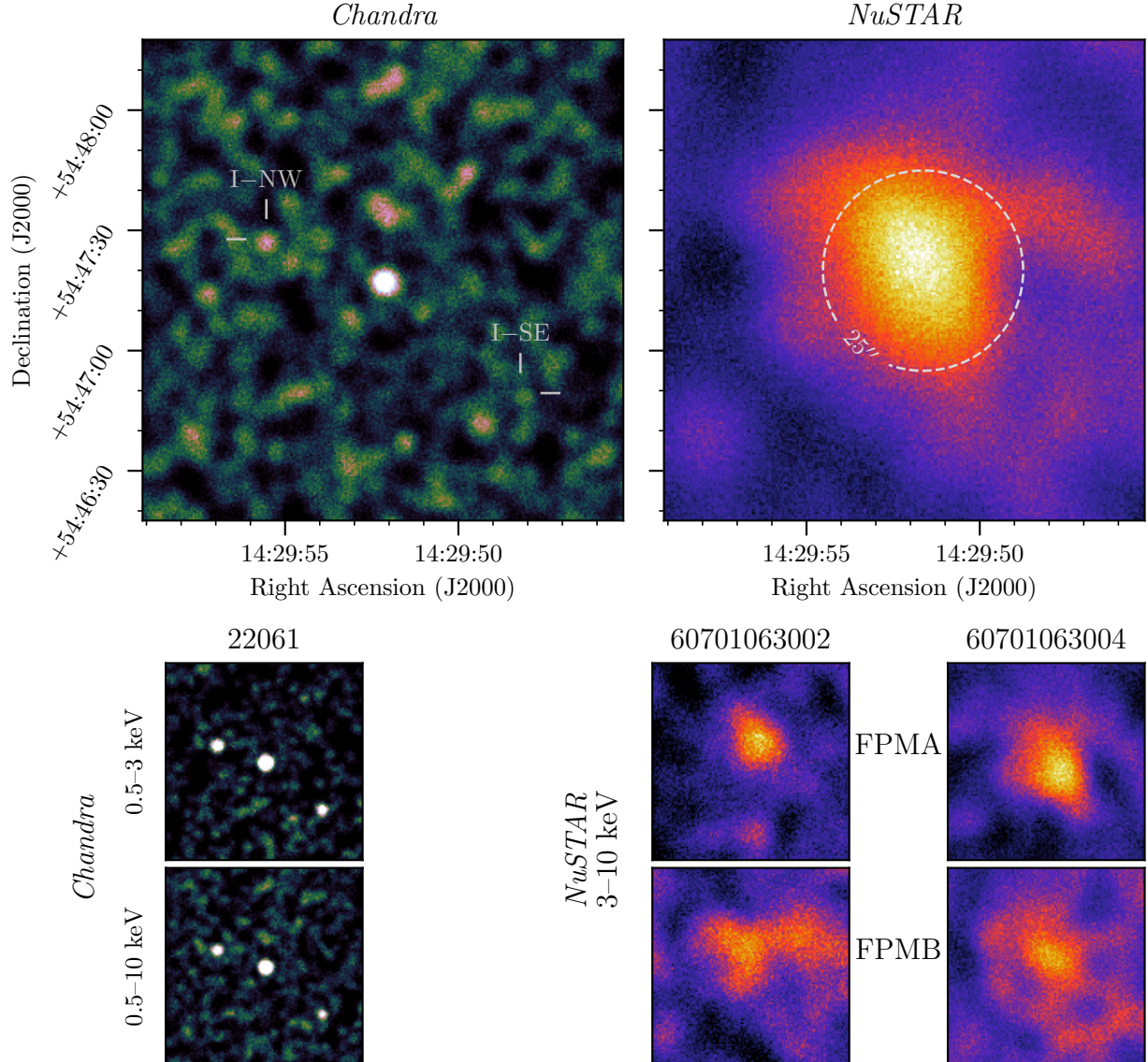


Figure 1. *Chandra* (left) and *NuSTAR* (right) X-ray observations of J1429+5447. All panels show the same $2' \times 2'$ region, and the sets of images are smoothed by Gaussian kernels of radius $2''$ (*Chandra*) and $8''$ (*NuSTAR*). **Top:** 3–10 keV images of the single *Chandra* observation and the combined *NuSTAR* observation. Reticles on the *Chandra* image mark the positions of I-SW and I-NE. A circular aperture of radius $25''$ is drawn around the centroid of the *NuSTAR* flux. **Bottom Left:** *Chandra* observations in a soft 0.5–3.0 keV band (upper) and broad 0.5–10.0 keV band (lower). The two interloper sources are clearly seen in these two bands, despite not contributing significant flux to the 3–10 keV band. **Bottom Right:** *NuSTAR* 3–10 keV images of J1429+5447 from observation 60701063002 (N02, left) and 60701063004 (N04, right) with FPMA (top) and FPMB (bottom). J1429+5447 is clearly detected in the combined image as well as the individual exposures, albeit less significantly in the FPMB images owing to the higher background.

in understanding their conditions and relating these insights to models of their growth.

Chief among these efforts is discovering more of these objects—more distant, more massive, and more complete samples. To date, hundreds of SMBHs have been found in the Epoch of Reionization (e.g. [Bañados et al. 2016, 2023](#); [Wang et al. 2019](#); [Matsuoka et al. 2022](#); [Fan et al. 2023](#)), with bil-

lion Solar mass black holes confirmed out to $z \gtrsim 7.5$ ([Bañados et al. 2018a](#); [Yang et al. 2020](#); [Wang et al. 2021a](#)) and spectroscopic mass measurements to $z \sim 10$ ($M_{\text{BH}} \approx 10^{6-7} M_{\odot}$, e.g., [Larson et al. 2023](#); [Maiolino et al. 2024a](#)). Detailed studies of these objects have provided critical information about their growth, including that the stellar populations of their host galaxies are undermassive ([Pacucci et al. 2023](#)), that broad-line region metallicity is established by $z \sim 7.5$ (e.g., [Onoue et al. 2020](#)), and that the first SMBHs reside in mas-

Table 1. X-ray Observations

Observatory	Instrument	ObsID	Effective Exposure (ks)	Start Date (YYYY-MM-DD)	CR _{3–5 keV} ^a (cts ks ⁻¹)	CR _{5–10 keV} ^a (cts ks ⁻¹)
<i>Chandra</i>	ACIS-S	22061	30.56	2021 Aug 03	0.446 ± 0.127	0.214 ± 0.124
<i>NuSTAR</i>	FPMA	60701063002 (N02)	78.3	2021 Nov 20	0.184 ± 0.067	0.235 ± 0.071
<i>NuSTAR</i>	FPMB	60701063002 (N02)	77.6	2021 Nov 20	0.138 ± 0.074	0.149 ± 0.085
<i>NuSTAR</i>	FPMA	60701063004 (N04)	166.4	2021 Nov 22	0.208 ± 0.046	0.263 ± 0.055
<i>NuSTAR</i>	FPMB	60701063004 (N04)	164.8	2021 Nov 22	0.117 ± 0.047	0.167 ± 0.057

^aCount rates are of J1429+5447 and are background-subtracted within apertures of radius 5'' (*Chandra*) and 25'' (*NuSTAR*).

sive halos (e.g., Farina et al. 2022). However, some of the strongest insights into the ongoing accretion come from X-ray observations, which directly trace the accretion ongoing in the Active Galactic Nucleus (AGN) powering the emission.

Owing to both the significant luminosity distances and the effects of redshifting steep power-law spectra (Connor et al. 2020), even luminous quasars from the Epoch of Reionization often yield limited photon statistics (e.g., Bañados et al. 2018b), and insights into these populations sometimes rely on as few as three photons (Vito et al. 2019a; Connor et al. 2019). To that end, high-redshift X-ray astronomy is heavily dependent on extrapolating from lower-redshift insights, such as the observed correlation between power-law spectral slope Γ and accretion rate (Brightman et al. 2013; Trakhtenbrot et al. 2017; Ricci et al. 2018) or the scaling between UV luminosity and UV-to-X-ray spectral slope (Lusso & Risaliti 2016). At this epoch, however, to accurately characterize higher-energy relations such as that between coronal temperature and compactness, broader bandwidth is needed than what is currently achievable with instruments such as *Chandra* and *XMM-Newton*—despite their power in characterizing accretion regions (Fabian et al. 2015; Lanzuisi et al. 2019).

Much of the work on the X-ray properties of the first quasars therefore comes from stacking analyses and population statistics (Nanni et al. 2017; Vito et al. 2019b; Li et al. 2021; Wang et al. 2021b; Zappacosta et al. 2023). Buttressing these works is the benefit of redshift on observed times; for a source at redshift z , the time elapsed in the observer frame, t_{obs} , is related to the time in the rest-frame (t_{rest}) as $t_{\text{obs}} = t_{\text{rest}}(1 + z)$. Thus, observations spread across years only sample source variations on time scales of months, and even the longest continuous X-ray observations cover just a few hours of rest-frame variability. Nevertheless, we have already witnessed a few cases of fast (e.g. $t_{\text{rest}} \sim 250s$; Moretti et al. 2021) and extreme (flux decrease of a factor of > 7 in $t_{\text{rest}} \sim 115$ days; Vito et al. 2022) X-ray vari-

ability of $z > 6$ quasars, shedding a light onto the physical processes powering these AGN.

It is this context that greeted the X-ray detection of CFHQS J142952+544717 (hereafter J1429+5447), a $z = 6.19$ (Khusanova et al. 2022) quasar first discovered by Willott et al. (2010). Powered by a black hole with a Mg II-derived mass measurement of $\log(M_{\text{BH}}/M_{\odot}) = 9.26 \pm 0.37$ (Shen et al. 2019), the quasar is radio-loud but shows no extended radio structure beyond 100 pc in projection (Frey et al. 2011). The source was detected by *SRG/eROSITA*¹ in 160 s (Medvedev et al. 2020); follow-up *XMM-Newton* observations confirmed this detection, and established that J1429+5447, with a 1.4 – 72 keV (rest-frame) luminosity of $L_{\text{X}} = 5.5_{-0.6}^{+0.8} \times 10^{46}$ erg s⁻¹, is far and away the most X-ray luminous object in the Epoch of Reionization (Medvedev et al. 2021; Migliori et al. 2023), surpassing runners-up SDSS J010013.02+280225.8 ($z = 6.3$, Connor et al. 2021a) and PSO J030947.49+271757.31 ($z = 6.1$, Belladitta et al. 2020) by around an order of magnitude.

Not only is J1429+5447 X-ray luminous, it is also radio-loud (radio-loudness parameter $R = f'_{\nu, 5\text{GHz}}/f'_{\nu, 4400\text{\AA}} = 109 \pm 9$ and $L_{5\text{GHz}} = 10^{9.6} L_{\odot}$; Kellermann et al. 1989; Bañados et al. 2015), a feature typically associated with strong jets. Despite [C II] observations (Khusanova et al. 2022) showing evidence for an AGN-driven outflow, Frey et al. (2011) found that the size of the resolved radio emission is only around 100 pc in projection and measured a 2-point (1.6–5 GHz) radio spectral index of $\alpha \sim -1.0$ (see also Coppejans et al. 2017); together, along with the relatively low rest-frame brightness temperature, these observations disfavor a blazar interpretation (i.e. the AGN hosts a relativistic jet pointed close to our line of sight, Urry & Padovani 1995). Conversely, recent CO spectral line energy distribution (SLED) observations seem to imply that the host

¹ J1429+5447 is located in the Eastern Galactic hemisphere, the side where analysis of eROSITA data is led by the Russian consortium.

galaxy could be strongly impacted by its jets (Khusanova et al., submitted, although cf. Li et al. 2024). The lack of observed large ($> \text{kpc}$ scale, Mingo et al. 2019) radio jets may be because jet emission is dominated by cosmic microwave background (CMB) photons being inverse Compton scattered (IC/CMB; e.g., Ghisellini et al. 2014, 2015). Such X-ray-dominated jets could potentially be tracers of needed rapid accretion (Jolley & Kuncic 2008), but detections of extended X-ray jets at these redshifts have been so-far limited (Connor et al. 2021b; Ighina et al. 2022) and may remain so until the next generation of X-ray satellites is launched (Connor et al. 2024; Marcotulli et al. 2024).

J1429+5447, at the extremes of the early Universe, is thus mystifying: radio-loud and X-ray luminous, but with neither extended jets nor the hallmarks of being a blazar. Yet its brightness makes it accessible at very hard energies ($E'_{\text{rest-frame}} > 50 \text{ keV}$), where AGN emission can be more easily isolated. We therefore obtained *NuSTAR* observations of the quasar to constrain possible X-ray emission scenarios that could be producing such extreme luminosity. In this paper we describe these observations, as well as the role of short-term variability from J1429+5447 in comparison to independent *Chandra* observations and the potential origins—and impacts—of that variability.

Throughout this work, we use a flat cosmology with $H_0 = 70 \text{ km s}^{-1} \text{ Mpc}^{-1}$, $\Omega_M = 0.3$, and $\Omega_\Lambda = 0.7$. We adopt a redshift for J1429+5447 of $z = 6.19$, as reported from [C II] line measurements by Khusanova et al. (2022); at this redshift, the scale is $5.61 \text{ kpc arcsec}^{-1}$. Per HIPI Collaboration et al. (2016), we assume a Galactic neutral hydrogen column density of $N_{\text{H}} = 1.15 \times 10^{20} \text{ cm}^{-2}$ in the direction of J1429+5447. All distances given are in proper distances and errors are reported at the 1σ (68%) confidence level unless otherwise stated. For reported radio spectral slopes, we follow the convention of $S_\nu \propto \nu^\alpha$; we instead use Γ for the reported X-ray photon indices following the convention $dN/dE \propto E^{-\Gamma}$ (where $\Gamma = \alpha - 1$).

2. OBSERVATIONS AND DATA REDUCTION

In this work we consider two sets of X-ray observations: archival *Chandra* imaging and new *NuSTAR* data. The summary of these observations, including the background subtracted count rates, can be found in Table 1. There are two X-ray interlopers in this field which impact these observations, which are discussed below. The coordinates and redshifts of these interlopers and the quasar J1429+5447 are given in Table 2.

2.1. Interloper Sources

There are two known X-ray interlopers in this field. The first, identified with *XMM-Newton* by Medvedev et al. (2021), is approximately $45''$ southwest of the quasar, while

Table 2. X-ray Sources

Name	R.A.	Dec.	Redshift
J1429+5447	14:29:52.18	+54:47:17.6	6.190 ± 0.004
I-SW	14:29:48.21	+54:46:49.1	1.23 ± 0.50
I-NE	14:29:55.54	+54:47:27.8	1.02 ± 0.13

References—J1429+5447’s redshift is from a fit to the [C II] $\lambda 158 \mu\text{m}$ line (Khusanova et al. 2022), while the interlopers’ redshifts are photometric (Duncan 2022).

the second, identified in higher-resolution *Chandra* imaging by Migliori et al. (2023), is roughly $30''$ to the quasar’s northeast. For clarity, we refer to these interloping sources as “I-SW” and “I-NE,” respectively, throughout this work. Using the robust *Chandra* astrometry, we cross-matched the positions of these sources with the *Hubble* Source Catalog (Whitmore et al. 2016), the Canada-France-Hawaii Telescope Legacy Survey (CFHTLS, Cuillandre et al. 2012), and the Legacy Imaging Surveys photometric redshift catalog of Duncan (2022). Neither source has a radio detection within $10''$ indexed by VizieR (Ochsenbein et al. 2000).

I-SW has NIR magnitude of $F105W = 22.4$, CFHTLS color of $i' - z' \approx 0.2$, and photometric redshift 1.23 ± 0.50 . I-NE has magnitude $F105W = 21.5$, color $i' - z' \approx 0.9$, and photometric redshift 1.02 ± 0.13 . In contrast, the CFHTLS color of J1429+5447 is $i' - z' \approx 2.5$, owing to the presence of the Lyman α break around 8740 \AA , significantly suppressing flux in the i' band. Because the tell-tale sign of the Lyman α break is not present, and in conjunction with the photometric redshifts, we conclude that these are foreground interloper sources, unrelated to the quasar or its system.

2.2. Chandra

J1429+5447 was observed by the *Chandra* X-ray Observatory for 30.56 ks on 2021 Aug 03 using the Advanced CCD Imaging Spectrometer (ACIS; Garmire et al. 2003). In the rest-frame of the quasar, these observations took place approximately 15 days before the *NuSTAR* observations. The quasar was positioned on the back-illuminated S3 chip, and ACIS was operated in the Timed Exposure (TE) mode with Very Faint (VF) telemetry saturation limits. These data, consisting of a single observation, are contained in CDC 308 and were previously published by Migliori et al. (2023).

We reduce the same observation using the *Chandra* Interactive Analysis of Observations software package (CIAO; Fruscione et al. 2006) v4.14 with CALDB v4.15. We define circular source regions of $5''$ radius centered, respectively, at the position of the quasar, I-NE, and I-SW. Annulus background regions of $7''$ inner and $23''$ outer radii centered at

the source locations are selected. The spectra for all three sources are obtained with the `specextract` function, and the spectral files are binned with the optimal binning scheme of `ftgrouppha` (Kaastra & Bleeker 2016). We fit our spectra with BXA (see Section 4.1) and compare our results to those of Migliori et al. (2023). Modulo uncertainties, neither I-NE or I-SW is brighter than J1429+5447, nor do they have shallower spectra; as such, and as evidenced by Figure 1, their contribution to the hard band probed by *NuSTAR* should be negligible—although we nevertheless include both sources in our fits.

2.3. *NuSTAR*

We observed J1429+5447 with *NuSTAR* (Harrison et al. 2013) as part of program 7291. These observations were split into two segments: an effective exposure time of 78.3 ks (FPMA) and 77.6 ks (FPMB) starting on 2021 Nov 20 (ObsID: 60701063002, hereafter referred to as N02) and 166.4 ks (FPMA) and 164.8 ks (FPMB) starting on 2021 Nov 22 (ObsID: 60701063004, hereafter referred to as N04). Although these observations were both preceded and separated by Solar observations in support of a *Parker* Solar Probe perihelion passage, instrumental temperatures were all within typical operating parameters for the duration of the observations and no problems were identified in quality assurance monitoring.

The *NuSTAR* observations were analysed using the most recent *NuSTAR* calibration database (CALDB) v. 2024-03-25 and HEASOFT v. 6.32.1. The data were pre-processed using the standard `nupipeline` routine. Although the source is very faint in the full 3–80 keV *NuSTAR* band, the 3–10 keV images (Figure 1) show a clear excess at the location of the source, in both observations and in both modules.

Since the *NuSTAR* PSF is large with respect to that of *Chandra* (FWHM of 18'' vs. 0.5''), the emission visible in the *NuSTAR* image may be due to a combination of J1429+5447, I-SW, and I-NE. Ideally, for our analysis, we would prefer to select a source region that encompasses both the location of the quasar and the interlopers; their measured separations (as can be seen in Figure 1) require that a circular region have a radius of at least 49'' to include all three sources. A radial profile of the *NuSTAR* images generated using the *NuSTAR* General Utilities² at the emission centroid location does not help us differentiate between one or multiple sources contributing to the *NuSTAR* counts within a 49'' radius due to the low number of source counts. However, most of the source counts in the *NuSTAR* image are concentrated in a circular region of radius $\sim 25''$, which, if selected as our source region

extent, maximizes the signal-to-noise of the data at hand and therefore improves our fit statistics³.

We therefore extracted spectra using both a signal-optimized circular region ($r = 25''$) and a more inclusive circular region ($r = 49''$) that covers the positions of both interloper sources. Both regions were centered on the centroids of the counts in the *NuSTAR* image (which corresponds to the coordinates of J1429+5447 to within 7''). Backgrounds were extracted from a circular region of radius 50'' for the smaller source region and 80'' for the larger source region, located away from source contamination but within the same detector area. The spectra of both source and background regions were computed using the `nuproducts` routine, and consistently the spectral files were binned with the optimal binning scheme of `ftgrouppha`.

3. X-RAY FITTING WITH BXA

J1429+5447 is clearly detected in both the *Chandra* and *NuSTAR* observations. However, its observed faintness requires our analysis to be fine-tuned to the low-count statistics regime. To properly account for the Poisson nature of the data without background modeling, we minimized the modified C-statistic (W-stat; Cash 1979; Wachter et al. 1979). We use the Bayesian X-ray Analysis (BXA, v.4.1.1, Buchner et al. 2014; Buchner 2016) software package that links the nested sampling algorithm `UltraNest` (v. 3.5.7, Buchner 2021) with the X-ray Spectral Analysis software `XSPEC` (Arnaud 1996; Gordon & Arnaud 2021). Here we provide a brief overview on how nested sampling works; further, specific details can be found in Buchner (2023).

To each of the fitted parameters of the tested model, we assign a prior distribution of possible values stored as a vector by the nested sampling algorithm. Then the likelihood space of the parameters' combination is explored iteratively, with the lowest likelihood parameter vector being replaced by a new one which has a higher likelihood value. This scan terminates when the contribution to the Bayesian evidence integral stabilizes and the likelihood weighted with the volume removed is negligible (see Section 3.4.2 of Buchner & Boorman 2023). The choice of priors depends on the fitted models and free parameters. In our specific case, where we use power-law-like models to fit our sources, we assign uniform priors to the spectral indices and log-uniform priors to the intrinsic normalizations. When fitting the simultaneous *NuSTAR* observations (see Section 4.2), we include a cross-

² <https://github.com/NuSTAR/nustar-gen-utils>

³ The radial profile of the source in the 3–10 keV energy range shows that the net count rate drops by a factor $\sim 1/e$ after $\sim 25''$ from the centroid location, and the signal-to-noise profile does not improve enlarging the source region to 49''.

Table 3. Spectral Fits

<i>Chandra</i>					
Source	Model	$N_{H,z}$ ($\times 10^{22} \text{ cm}^{-2}$)	Γ	$\log(F_{0.5-10 \text{ keV}})$ [$\text{erg cm}^{-2} \text{ s}^{-1}$]	$\log(F_{3-7 \text{ keV}})$ [$\text{erg cm}^{-2} \text{ s}^{-1}$]
J1429+5447	M1	...	$2.32^{+0.15}_{-0.33}$	$-13.25^{+0.04}_{-0.06}$	$-13.92^{+0.10}_{-0.11}$
I-NE	M2	$19.02^{+6.89}_{-8.09}$	$3.58^{+1.54}_{-0.49}$	$-13.93^{+0.09}_{-0.12}$	$-14.45^{+0.21}_{-0.20}$
I-SW	M1	...	$2.20^{+0.41}_{-0.83}$	$-13.92^{+0.12}_{-0.12}$	$-14.48^{+0.29}_{-0.14}$
<i>NuSTAR</i>					
Observation	Module	Model	const	Γ	$\log(F_{3-78 \text{ keV}})$ [$\text{erg cm}^{-2} \text{ s}^{-1}$]
60701063002	FPMA	M1	1 (fixed)	$2.34^{+0.68}_{-0.73}$	$-13.14^{+0.18}_{-0.19}$
60701063002	FPMB	...	$0.96^{+0.11}_{-0.07}$
60701063004	FPMA	M1	1 (fixed)	$2.49^{+0.42}_{-0.24}$	$-13.08^{+0.09}_{-0.10}$
60701063004	FPMB	...	$0.88^{+0.10}_{-0.08}$
Joint <i>Chandra</i> and <i>NuSTAR</i>					
Instrument	Source	Model	$N_{H,z}$ ($\times 10^{22} \text{ cm}^{-2}$)	Γ	$\log(F_{3-7 \text{ keV}})$ [$\text{erg cm}^{-2} \text{ s}^{-1}$]
<i>Chandra</i>	J1429+5447	M1	...	$2.22^{+0.31}_{-0.12}$	$-13.95^{+0.11}_{-0.08}$
	I-NE	M2	$16.59^{+4.78}_{-5.63}$	$3.39^{+0.48}_{-0.44}$	$-14.35^{+0.12}_{-0.16}$
	I-SW	M1	...	$1.73^{+0.42}_{-0.48}$	$-14.45^{+0.25}_{-0.17}$
Co-added FPMA	J1429+5447	M1	...	$2.22^{+0.60}_{-0.54}$	$-13.49^{+0.07}_{-0.10}$

NOTE—The values reported in the Table are the mode and the 68% confidence level obtained from the posterior distribution of the parameters. The reported fluxes are the observed absorbed ones, i.e. we do not correct for the Galactic (or source) absorption. **Chandra:** We separately fit the three sources in the image: the quasar and I-SW with a redshifted powerlaw (M1, Section 3.1) and I-NE with an absorbed redshifted power-law (M2). **NuSTAR:** the *NuSTAR* observations are fit separately with a redshifted power law to test for day time-scale variability (see Section 4.2) over the full *NuSTAR* energy band (3–78 keV) using the spectral products obtained with a 25'' radius source region. Scaling between FPMA and FPMB was included through multiplicative constants. **Joint:** The *NuSTAR* data are fit as the sum of all three sources, with the interloper spectra fixed to the *Chandra* fits (see Section 4.3 for details).

calibration between the two detector modules; this parameter is fixed to 1 for FPMA and assigned a custom log-Gaussian prior with mean zero (i.e. a linear cross-calibration of unity, Madsen et al. 2017) and 0.1 standard deviation for FPMB. When fitting non-simultaneous observations from different instruments, the cross-calibration constants are a binary flag used to turn different components of the fit on or off (see Section 4.3, and Appendix A for more details).

3.1. Tested models

For the sake of clarity and reproducibility, we list here the XSPEC spectral model used in the next sections.

- **M1:** A redshifted power law
`const*tbabs*zpowerlaw`
- **M2:** An absorbed redshifted power law
`const*tbabs*ztbabs*zpowerlaw`
- **M3:** A redshifted broken power law
`const*tbabs*zbknpower`
- **M4:** A redshifted power law with exponential cutoff
`const*tbabs*zcutoffpl`

The Galactic absorption is frozen at the Galactic value ($N_{\text{H}} = 1.15 \times 10^{20} \text{ cm}^{-2}$, HI4PI Collaboration et al. 2016) with the `tbabs` XSPEC model. The chemical abundance is

set to that of Wilms et al. (2000, `wilm`). Throughout the paper, we report the mode of each parameter distribution alongside the highest density interval (HDI) at the 68% level as our uncertainty, extracted on the posterior distribution for each of the fitted parameters. Finally, for every combination of parameters in the posterior distribution, we can derive the posterior distribution of flux and luminosity for every tested model in any desired energy band; the mode and HDI (68%) of these distributions are quoted in the paper as our source’s flux and luminosity.

4. RESULTS

4.1. *Chandra*

Our first objective was to establish X-ray properties for the three sources seen in the *Chandra* observations to ensure the differences in reduction and analysis from the work of Migliori et al. (2023) had no systematic effects. To that end, we fit the existing *Chandra* data in the 0.5–7.0 keV band for all three sources; for J1429+5447 and I-SW we used the redshifted power law (M1, Section 3.1), while, since I-NE shows hints of an extra absorber (Migliori et al. 2023), we fit it with a redshifted power law with an intrinsic, redshifted absorber (M2). Adopted redshifts for these sources are given in Table 2. The results of these fits are given in Table 3.

In the case of J1429+5447 we recover a photon index of $\Gamma = 2.32^{+0.15}_{-0.33}$ and an observed unabsorbed flux in the 0.5–10 keV range of $F_{0.5-10\text{ keV}} = 5.6^{+0.6}_{-0.7} \times 10^{-14} \text{ erg cm}^{-2} \text{ s}^{-1}$, completely consistent with the results in Migliori et al. (2023). The results on I-SW also agree within errors with what is reported in Migliori et al. (2023, cf. Table 1 of their work). We find that for I-NE the column density of the extra absorber is $\sim 1.9 \times 10^{23} \text{ cm}^{-2}$, indicating that the source is intrinsically obscured at soft X-ray energies. The derived photon index, $\Gamma_{\text{I-NE}} = 3.39^{+0.48}_{-0.44}$, is quite soft though consistent within 3σ to the values reported in Migliori et al. (2023). The differences in spectral parameters—mostly limited to absorption—found over the results of Migliori et al. (2023) can be explained by the fact that we include the redshift of the interloper, while the earlier analysis did not; the recovered X-ray flux of the interloper is consistent within statistical uncertainties.

4.2. *Independent NuSTAR Observations*

Although the start times of the two *NuSTAR* observations are separated by two days, there is only a gap of roughly seven hours between the end of N02 and the start of N04. Nevertheless, we fit both observations independently, both to compare the derived properties of our two source extraction regions and to search for rapid variability. For both observations, we fit the observed spectra with a redshifted power law (M1) over the full 3–78 keV range, with FPMA and

FPMB linked within each observation by a freely-varying cross-normalization coefficient.

We separately fit both the 25'' and 49'' radius extraction region spectra, with the results of the former shown in Table 3. When using the larger region, we found no meaningful change in flux or spectral index, but the lower signal-to-noise results in larger statistical uncertainties. As such, we do not use the spectra extracted with the larger regions in further analysis. Additionally, as shown in Table 3, there is no detectable variability between the two *NuSTAR* observations, either in flux or in spectral shape. Furthermore, the cross-calibration constants between the *NuSTAR* modules are consistent with unity, within errors. For subsequent fits, we opted to co-add the FPMAs from both observations with the python wrapper of the FTOOL `addspec`⁴, binning them with `ftgrppha` using the optimal binning.

Moreover, we decided to not include the FPMB observations as the source was located in a region of the *NuSTAR* field of view in which the aperture background contribution is higher in FPMB than the corresponding location in FPMA (see Figure 1). The different background levels for the two FPMs can cause issues when the difference in backgrounds is comparable to the flux of the source (Wik et al. 2014; Greenwell et al. 2024). This choice reduces the dimensionality of the parameter space explored by BXA, thus dramatically decreasing computational time, without impacting our findings in a statistically meaningful way. We note that limiting our analysis to *NuSTAR* data below 15 keV gives statistically indistinguishable results, as the W-statistic allows us to fit background-dominated spectral regions (Buchner & Boorman 2023).

4.3. *Combined Chandra and NuSTAR*

Separated by ~ 110 days in the observed frame, the *Chandra* and *NuSTAR* observations sample any potential variability on rest-frame scales of ~ 15 days (Lewis & Brewer 2023). To test for such variability, we performed a simultaneous fit on both data sets, including all three sources in the *Chandra* observations and the single extraction in the co-added *NuSTAR* FPMA observation. We modeled all three sources as for the *Chandra*-only observations: redshifted power laws (M1) for J1429+5447 and I-SW and an absorbed redshifted power law (M2) for I-NE. Fits were over the 0.5–7.0 keV (*Chandra*) and 3–78 keV (*NuSTAR*) ranges.

In total, the fit was composed of six models: J1429+5447 I-NE, and I-SW, fit independently for their *Chandra* spectra and in combination for the *NuSTAR* spectrum. The values for the two interloper sources were linked between observatories, under the assumption that these sources did not meaningfully vary over the observed time difference (see dis-

⁴ <https://github.com/JohannesBuchner/addspec.py>

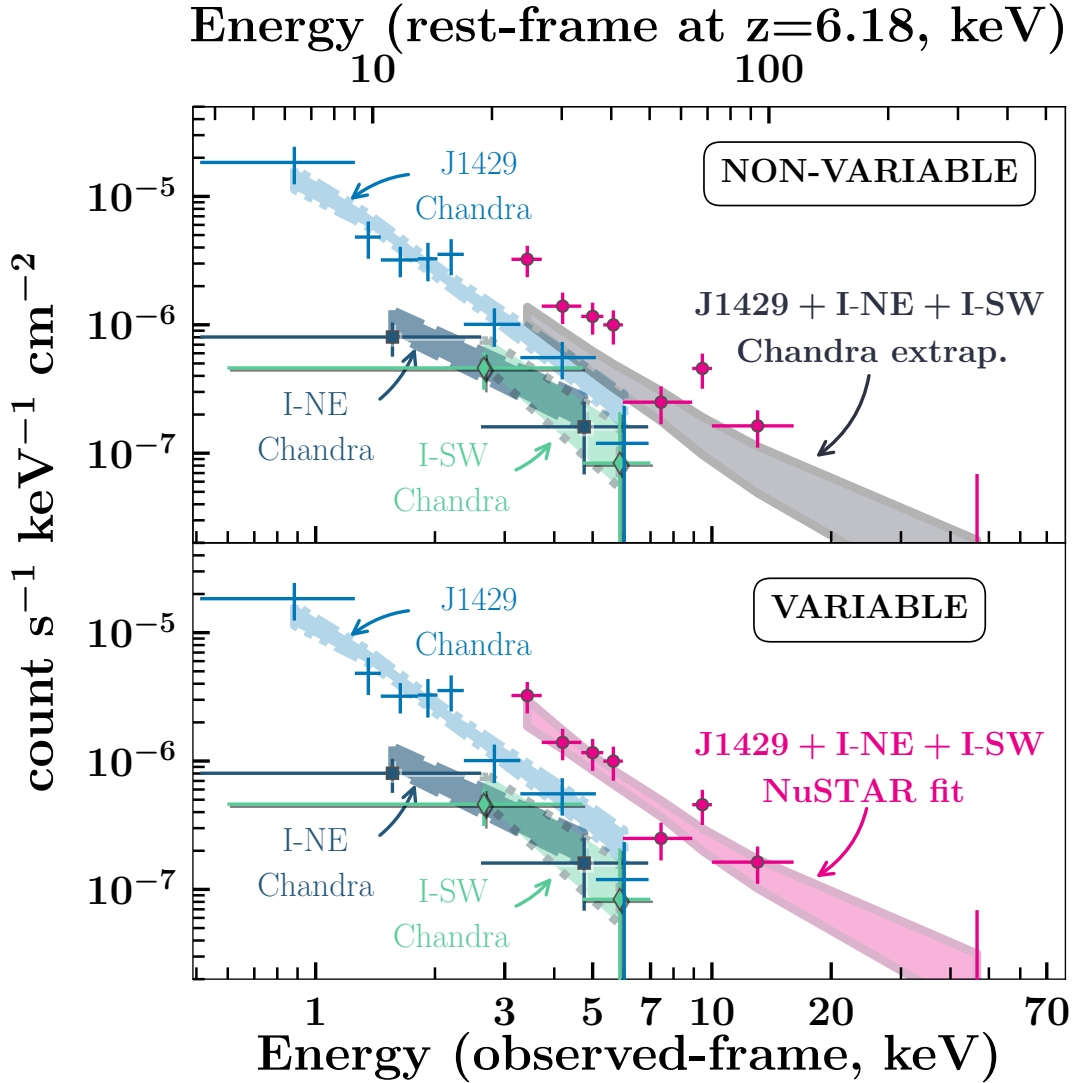


Figure 2. Background-subtracted counts spectra for all three *Chandra* sources (J1429+5447, light-blue crosses; I-NE, navy squares; I-SW, green diamonds) and the *NuSTAR* data (fuchsia points), after binning each spectrum to have a minimum significance of three per bin for visual clarity. Source counts are not unfolded through the model but are instead normalized by the average effective area in each bin. In both panels, we show the model predictions for the fits to the *Chandra* data of J1429+5447 (light blue, dash-dotted lines), I-NE (navy, dashed line), and I-SW (green shade, dotted line). The shaded bands in the plot represent the 68th percentile range regions of model predictions, as calculated from our posteriors. The **top** panel shows the *Chandra*-only fits extrapolated (and summed) into the *NuSTAR* passband (gray shade, solid line), which is representative of the scenario in which none of the sources are variable; the **bottom** panel instead shows the result of our fit in which J1429+5447 was allowed to vary in its normalization and photon index between the *NuSTAR* and *Chandra* epochs (fuchsia shade, solid line), under the assumption that I-NE and I-SW did not vary in the 4 months (observed frame; < 2 months rest-frame assuming their photometric redshifts in Table 2) between the two observations. The results indicate that the J1429+5447 X-ray flux varied by a factor of 2.6 at > 90% CL (see also Figure 3).

cussion in Section 5.2.4). Although the interlopers were not centered in the *NuSTAR* aperture, we conservatively included their entire flux in the *NuSTAR* spectra. For J1429+5447, however, both the normalization and photon index were free to vary independently in both observations. BXA fits return the posterior distribution of parameters for all components, and so, for each set of posteriors, we can extract flux measurements in any desired energy band, although we focus on the overlapping 3–7 keV range.

The results of our fit are presented in Table 3; we find that J1429+5447 increased in flux by roughly 0.4 dex between observations. We show the background-subtracted unfolded spectra, best fits, and uncertainties in Figure 2. To further demonstrate the extent of the flux change, we plot the posterior distributions of Γ and $F_{3-7 \text{ keV}}$ in Figure 3. For both Figures 2 and 3, we stress that the *NuSTAR* posteriors obtained for J1429+5447 depend on the posteriors of all other *Chandra* components.

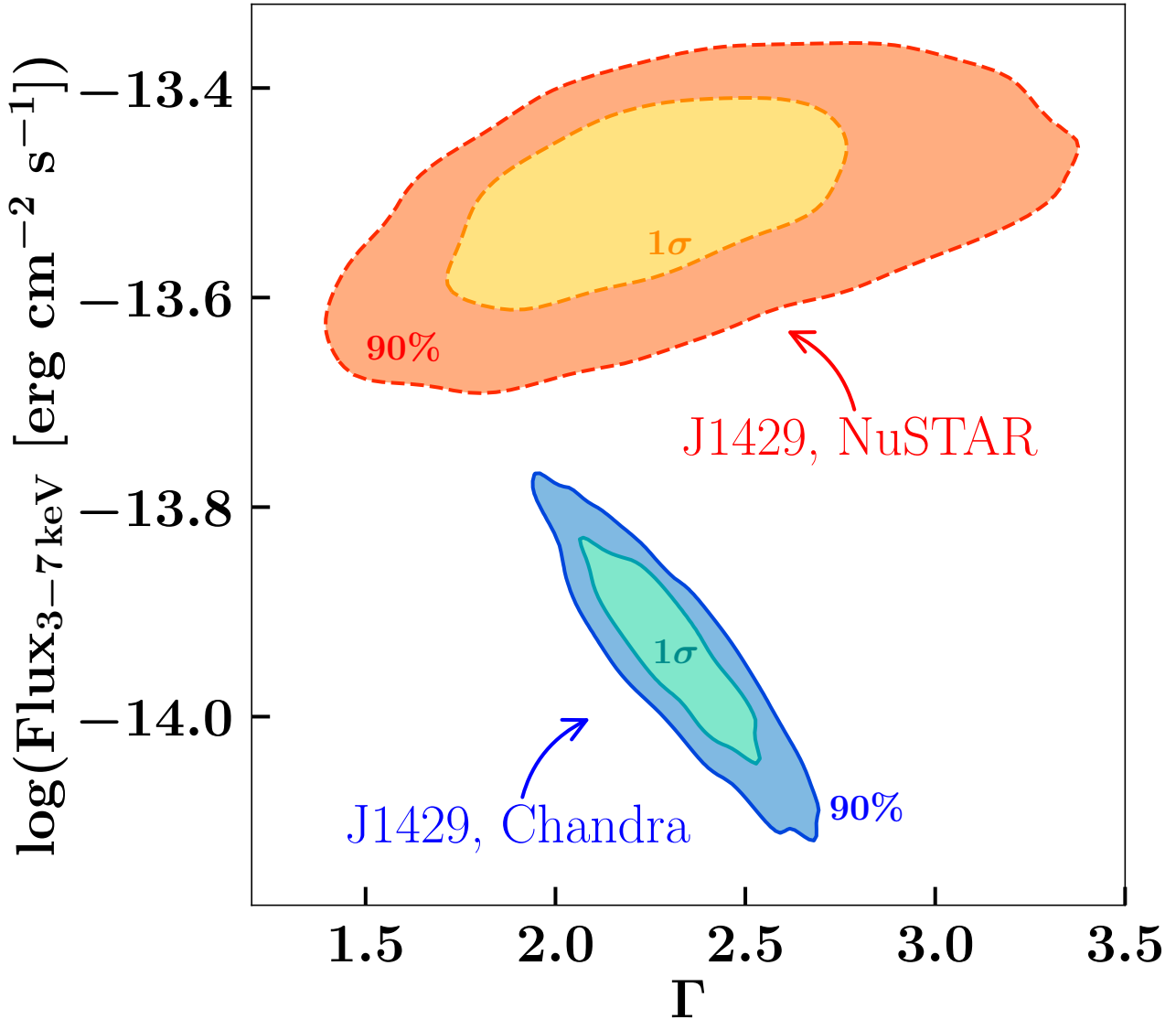


Figure 3. 3 – 7 keV posterior flux distribution versus the full-band photon index posterior distribution for J1429+5447 obtained with the simultaneous fit of the three *Chandra* sources and the co-added *NuSTAR* FPMAs (details in Section 4.3). The 1σ and 90% contour levels are reported in the plot. There is no overlap between the two contours, which is a further indication that the flux of the source varied in the four months (observed frame) between observations. The photon index distributions span a similar range, indicating that more likely the source only varied in flux. Note that these photon indices are extracted by fitting datasets covering different energy ranges, and hence cannot be compared one-to-one.

The posterior distributions shown in Figure 3 do not overlap within their 90% confidence intervals, indicating that the flux varied at a statistically significant level. But not only do the two distributions not overlap, the value of flux they encompass does not overlap, either—such that they do not allow for a scenario in which the flux remained constant while the spectral shape varied. To better demonstrate this effect, we plot the distribution of flux offsets (in effect marginalizing over the values of Γ) in Figure 4. We find an average logarithmic flux increase in the 3–7 keV band, $\log(F_{NuSTAR}/F_{Chandra})$, of 0.42, with a one-tailed 90%

lower limit of 0.24. The magnitude of this offset relative to typical AGN behavior is discussed in Section 5.2.1.

4.4. More Complex Models

The harder energies probed by the *NuSTAR* observations mean that, in comparison to previous *XMM-Newton* or *Chandra* observations, we could potentially observe more complex features arising in the observed spectra beyond a simple power law. For example, for X-ray emission produced solely by the AGN corona, we would expect to see a coronal cut-off at high energies—potentially observable by *NuSTAR* (e.g. Ricci et al. 2017; Baloković et al. 2020; Kammoun et al.

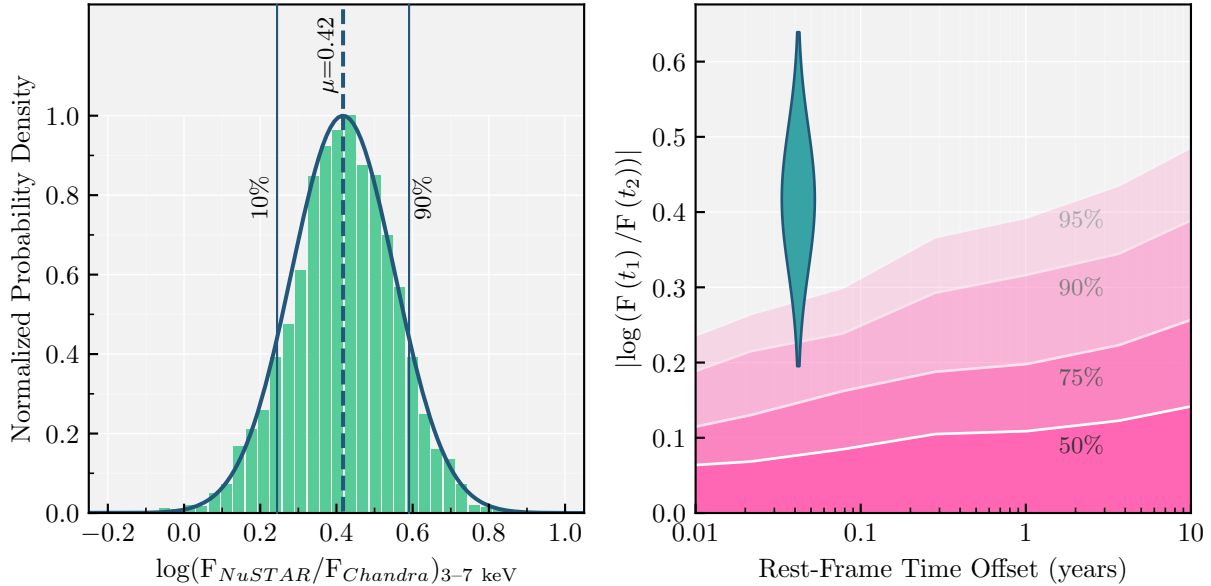


Figure 4. **Left:** Histogram of the difference between the *Chandra* and *NuSTAR* 3–7 keV posterior flux distribution obtained by simultaneously fitting all three *Chandra* data sets and the *NuSTAR* co-added FPMA. The mean (dashed vertical line) and 90% confidence limit (CL, solid vertical lines) of the distributions obtained by a Gaussian fit (solid line) are shown. This histogram highlights that J1429+5447 varied in flux between the *Chandra* and *NuSTAR* epoch of observation at > 90% CL. The mean of the distribution indicates that the *NuSTAR* flux is ~ 2.6 times higher than the *Chandra* one. Moreover, only 0.26% of the distribution has a value ≤ 0 , in support of the fact that it is highly unlikely that the source did not vary between the two epochs. **Right:** 90% distribution of flux offsets observed for J1429+5447 (dark blue-green) relative to flux offsets observed for lower-redshift ($z = [1, 2]$) AGN in a broadly similar regime of black hole masses ($M_{\text{BH}} > 10^8$) and Eddington ratios ($\lambda_{\text{Edd}} > 0.01$) by Georgakakis et al. (2024, from dark to light pink). Most of the probability distribution of observed brightening occupies the region where fewer than 5% of comparison flux variations reside. The rapidity of such a significant flux offset is thus unusual for an AGN.

2024). Such cut-offs are markers of the nature of the X-ray emitting particles and coronal physics. Conversely, the soft energies may be biased, such as by a Compton hump, with the harder energies better tracing the coronal emission (e.g. Torres-Albà et al. 2021; Boorman et al. 2024). Alternatively, if the emission is coming from a jet, we could see a softening at higher energies in the spectrum if we were sampling the peak and/or the high-energy tail of the electron energy distribution producing the visible emission (radiating either via external Compton or synchrotron self-Compton processes; e.g., An & Romani 2018, 2020; Marcotulli et al. 2020, 2022; Moretti et al. 2021; Sbarrato et al. 2022; Gokus et al. 2024).

Owing to the fact that BXA enables us to sample the full parameter space for different models, and hence to discern which part of the parameter space is allowed given our data, we tested these more complex models by fitting J1429+5447 with

1. a redshifted, broken power law (M3; Section 3.1) and
2. a redshifted power law with an exponential cut-off (M4; Section 3.1).

As done for the simple power law case (Section 4.3), *Chandra* spectra of I-SW and I-NE were also included in the fit.

Our results show that the fits of the observed spectra to these more complex models are not favored by the data (see Appendix B for details on the spectral fit results). In particular, the photon indices found through these fits are consistent with that of the simple power law case (M1). Nevertheless, the posterior distributions of these fits enable us to establish a lower-limit to the location of the possible spectral cut-off, $E_{\text{cut,obs-frame}} \geq 23.6 \text{ keV}$, or equivalently $E'_{\text{cut,rest-frame}} \geq 169 \text{ keV}$. Such a value is only slightly constraining given the luminosity of the source (e.g., Molina et al. 2019). However, the uncertainties in the fit parameters and residuals do not indicate an improvement with respect to the power-law fit.

5. DISCUSSION

The detection of J1429+5447 with eROSITA (Medvedev et al. 2020) marked not just one of the most distant AGN detected in X-rays (e.g., Ai et al. 2016; Nanni et al. 2018; Bañados et al. 2018b; ?, Connor et al. 2019, 2020; Yang et al. 2022), but also the revelation that it was, by far, the most X-ray luminous source in the Epoch of Reionization. With a reported $L_{2-10 \text{ keV}} = 2.6^{+1.7}_{-1.0} \times 10^{46} \text{ erg s}^{-1}$, it is almost an order of magnitude brighter than other runner up $z > 6$ quasars (e.g. Belladitta et al. 2020; Connor et al. 2021a). Subsequent *XMM-Newton* observations confirmed this luminosity and

constrained the source’s spectral parameters (Medvedev et al. 2021), while additional high angular resolution *Chandra* observations provided additional insights, including the detection of two nearby X-ray sources unresolved by the original observation (Migliori et al. 2023). In this work we analyzed the first *NuSTAR* observations of this system; the hard energy spectrum is well described by a power law of $\Gamma_{3-78 \text{ keV}} = 2.22_{-0.54}^{+0.60}$, consistent with the observed *XMM-Newton* and *Chandra* spectral properties of the source. Importantly, we find to more than 90% confidence that the source flux varied over the observed four month baseline between *Chandra* and *NuSTAR* observations, at a level of $F_{\text{NuSTAR}}/F_{\text{Chandra}} = 2.6_{-0.7}^{+1.0}$. The derived *NuSTAR* broadband luminosity of the source in the 21.54 – 71.8 keV rest frame of the source is $L_{21.54-71.8 \text{ keV}} = 1.7_{-0.2}^{+0.5} \times 10^{46} \text{ erg s}^{-1}$; in the canonical 2 – 10 keV rest-frame, the quasar luminosity increased from $L_{2-10 \text{ keV, Chan.}} = (1.6 \pm 0.4) \times 10^{46} \text{ erg s}^{-1}$ to $L_{2-10 \text{ keV, NuS.}} = 4.1_{-1.6}^{+2.2} \times 10^{46} \text{ erg s}^{-1}$.

These results raise three questions, which we discuss in turn: what is the scale of the variability for J1429+5447, what could have caused such a rapid, intense increase in the X-ray flux, and what future insights are needed to better understand this and similar sources?

5.1. Scale of variability

The *NuSTAR* observations presented here are now the fifth reported X-ray flux measurements for J1429+5447, following two eROSITA observations (Medvedev et al. 2020 and Medvedev et al. 2021), the *XMM-Newton* follow-up (Medvedev et al. 2021), and the *Chandra* visit analyzed here (Migliori et al. 2023). There are also several other repeated observations in other wavebands that enable a check on the type of variability J1429+5447 displays.

To properly discuss these X-ray fluxes, we first convert previous measurements into the common 3–7 keV band. Medvedev et al. (2021) provide flux values for the two eROSITA observations: $F_{0.2-6 \text{ keV}} = 1.1_{-0.5}^{+0.6} \times 10^{-14}$ and $1.3 \pm 0.6 \times 10^{-14} \text{ erg s}^{-1} \text{ cm}^{-2}$ for epochs I and II, respectively. These values were extrapolated using the best-fitting model of Medvedev et al. (2021), with $\Gamma = 2.5$, which we, in turn, use to extrapolate flux values in our desired band. We find a first epoch flux of $F_{3-7 \text{ keV}}^{\text{I}} = (1.4 \pm 0.7) \times 10^{-14} \text{ erg s}^{-1} \text{ cm}^{-2}$ and second epoch flux $F_{3-7 \text{ keV}}^{\text{II}} = (1.6 \pm 0.7) \times 10^{-14} \text{ erg s}^{-1} \text{ cm}^{-2}$. Likewise, we use the fits presented in Medvedev et al. (2021) to re-derive a new *XMM-Newton* flux of $F_{3-7 \text{ keV}} = 1.3_{-0.2}^{+0.3} \times 10^{-14} \text{ erg cm}^{-2} \text{ s}^{-1}$.

We show these fluxes, as well as the newly measured *Chandra* and *NuSTAR* fluxes, in Figure 5. We note that only these two new data points account for the contamination of the two interlopers, and that the eROSITA and *XMM-Newton* points may thus be biased towards a higher flux value; indeed, although *XMM-Newton* observations re-

solved and excluded I-SW, Medvedev et al. (2021) used a spectral extraction region that includes I-NE (see discussion in Migliori et al. 2023, regarding the effect of I-NE of the *XMM-Newton* spectra). Nevertheless, aside from the *NuSTAR* observation, we find that the quasar flux has been otherwise stable, within uncertainties. The intra-*XMM-Newton* variability was tested by Medvedev et al. (2021) and further explored by (Migliori et al. 2023) in the context of the *Chandra* observations, with neither study finding any statistically significant variation. As such, there is no evidence that the X-ray flux of J1429+5447 varied significantly until the *NuSTAR* observation analyzed here.

As a radio-loud quasar, J1429+5447 has now been observed in three epochs by the Very Large Array Sky Survey (VLASS, Lacy et al. 2020). The measured 3 GHz flux densities are $2.01 \pm 0.13 \text{ mJy}$ (2017 December 01), $1.71 \pm 0.12 \text{ mJy}$ (2020 September 01), and $1.95 \pm 0.12 \text{ mJy}$ (2023 February 10). Again, no significant variability in the radio intensity is seen; if the *NuSTAR* excess is related to the radio emission, it is thus more likely to be of a flaring nature than of a continuous variation.

5.2. Origin of the Rapid Variability

5.2.1. AGN Variability

We first consider if this variability could be due to standard processes in AGN. Assuming coherent emission from a non-jetted AGN, the time scale of the variability constrains the size of the reprocessing component:

$$R \leq c \times \Delta t_{\text{rest-frame}}. \quad (1)$$

For J1429+5447, the ~ 15 rest-frame days offset corresponds to $R = 72 R_{\text{Schw}} \approx 0.01 \text{ pc}$, where the Schwarzschild radius for J1429+5447 is $R_{\text{Schw}} \sim 5 \times 10^{14} \text{ cm}$.

The X-rays in typical AGN are produced via inverse Compton scattering of accretion disk photons by a hot plasma of electrons known as the AGN corona (e.g. Haardt & Maraschi 1991). This primary X-ray spectrum, usually described by a power-law with an exponential cut-off, can also be reprocessed (and even absorbed) by material in the AGN surroundings—the accretion disk itself ($R_{\text{disk}} = 1 - 500 R_{\text{Schw}}$), the broad line region ($R_{\text{BLR}} \lesssim 0.1 \text{ pc}$), and the torus ($R_{\text{Tor}} \lesssim 10 \text{ pc}$). Assuming this is an adequate description for J1429+5447, the short variability timescale indicates that the most likely reprocessing component of the X-ray emission is the inner accretion disk and that the observed flux enhancement could be caused by variability in the corona itself or in the accretion flow (e.g. Ponti et al. 2012; Puccetti et al. 2014; Tortosa et al. 2023; Serafinelli et al. 2024). For example, if the accretion was (close to) super-Eddington, then timescale variation in the disk can happen on short timescales (see Discussion in Vito et al. 2022).

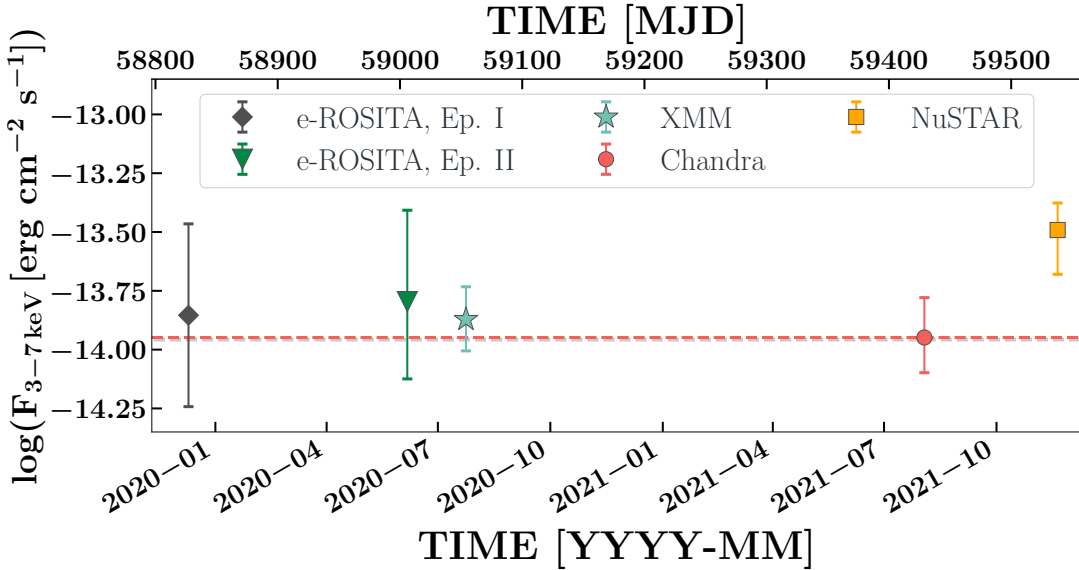


Figure 5. 3 – 7 keV light-curve of J1429+5447; the errors are the 90% HDI levels. The eROSITA flux points (black diamond & green triangle) are derived by extrapolating the spectrum to the 3 – 7 keV range using $\Gamma = 2.5$ and the eROSITA 0.2 – 6 keV fluxes reported in Medvedev et al. (2021). The *XMM-Newton* flux point (cyan star) was derived using the best-fit power law model of Medvedev et al. (2021). The *Chandra* (red dot) and *NuSTAR* (yellow square) data points are the ones obtained in this work. To guide the eye, the red dashed line at the level of the *Chandra* flux is plotted. This plot highlights that there was no evidence of variability for J1429+5447 before the *NuSTAR* observation, when the source flux brightened by 0.4 dex.

Considering the estimated lower limit on the luminosity of J1429+5447 below 2 keV from Medvedev et al. (2020, $L_{<2\text{ keV}} = 1.2 \times 10^{47} \text{ erg s}^{-1}$) and the 2–100 keV luminosity of the source from our newly derived fits, we estimate the bolometric luminosity of the quasar following Medvedev et al. (2020) to be

$$L_{\text{bol}} = L_{<2\text{ keV}} + L_{2-100\text{ keV}}. \quad (2)$$

We find $L_{\text{bol,Chan.}} \sim 1.4 \times 10^{47} \text{ erg s}^{-1}$ and $L_{\text{bol,Nu.}} \sim 1.8 \times 10^{47} \text{ erg s}^{-1}$. The black hole mass from Shen et al. (2019) gives us an Eddington luminosity of $L_{\text{Edd}} = 2.3 \times 10^{47} \text{ erg s}^{-1}$; therefore we can also relate the X-ray variability to an increase in Eddington ratio from $\log(\lambda_{\text{Edd}}) \sim -0.2$ to $\log(\lambda_{\text{Edd}}) \sim -0.1$, values consistent with the high-end tail of typical AGN Eddington rates (e.g. Suh et al. 2015). Hence, the accretion regime in the system—already quite fast—could have been slightly enhanced, leading to the observed increase of X-ray flux.

To put J1429+5447 in context with other AGN, in the right panel of Figure 4 we compare the observed flux variability amplitude and timescale of J1429+5447 with the observed variability seen in a broad sample of AGN, as compiled by Georgakakis et al. (2024). To compare to a sample of similar sources, we limit this analysis to black hole masses of $M_{\text{BH}} > 10^8 M_{\odot}$ and Eddington ratios of $\log(\lambda_{\text{Edd}}) > -2$; we also require at least five times the source counts than the expected background for each measurement. Although that work samples the 0.2–2.3 keV energy range, the self-similar nature of power laws means that logarithmic flux offsets will

be consistent with our chosen 3.0–10 keV band. As can be seen in Figure 4, the observed variability is extreme for that seen in similar AGN at similar time scales; if the flux variation comes from typical AGN processes, it would represent a significant statistical outlier.

One of the key results presented by Georgakakis et al. (2024) is that the amplitude of flux variation decreases with increasing mass and accretion rate; as such, not only is this comparison sample thus better suited than others that lack mass and Eddington ratio information (e.g., Timlin et al. 2020, which shows stronger typical flux variations), but, by extending more than a decade below J1429+5447 in mass and Eddington ratio, the sample is also conservative. While both the Georgakakis et al. (2024) and Timlin et al. (2020) analyses focus on radio-quiet quasars, J1429+5447 is radio-loud; although the expected amplitude of flux variations may be larger for radio-loud quasars, these variations are often attributed to jets or beaming (Carnerero et al. 2017)—topics we address below—rather than from the AGN and its corona.

The spectral index derived by our analysis is $\Gamma_{\text{NuSTAR}} = 2.22^{+0.60}_{-0.54}$, fully consistent with typical X-ray coronae in the local universe ($\Gamma = 1.8 - 2.0$, e.g. Ricci et al. 2017). Softer spectral behavior has been seen for AGN at the Epoch of Reionization (e.g., Vito et al. 2019b; Wang et al. 2021b; Zappacosta et al. 2023), hinting to either an evolution of intrinsic coronal spectral properties with redshift or a lower coronal temperature regulated by a hybrid thermal/non-thermal plasma (e.g. Coppi 1999). Ideally, if we were indeed look-

ing at the emission from an unobscured AGN, we would like to constrain the cut-off of the corona, often used to infer the coronal temperature. Our fit gives us a lower limit on the high-energy cut-off, $E_{\text{cut-off,rest-frame}} > 169$ keV, and an X-ray luminosity in the 2 – 10 keV band that increased from $L_{\text{Chandra}} = (1.6 \pm 0.4) \times 10^{46}$ erg s⁻¹ to $L_{\text{NuSTAR}} = 4.1_{-1.6}^{+2.2} \times 10^{46}$ erg s⁻¹. Our lower limit on the coronal cut-off energy agrees with the theoretical expectation (see Fabian et al. 2015; Lanzuisi et al. 2019) for a $10^9 M_{\odot}$ black hole with luminosities of J1429+5447 in either the slab or hemispheric coronal scenario, as well as the observational properties of other local AGN (where coronal cut-offs have been measured in the range $E_{\text{cut-off,rest-frame}} \gtrsim 100\text{--}500$ keV; e.g. Ricci et al. 2018; Baloković et al. 2020; Akylas & Georgantopoulos 2021). If present, it is likely that the turn-over happens in the spectral range dominated by the NuSTAR background ($\geq 20\text{--}30$ keV, observer frame), although this is currently unconstrained by our data quality.

An extreme possibility to consider is for the detected variability to have an obscuration-based origin. Indeed, Compton-thick BLR and/or outflow-based obscuration has been proposed to be more common at higher redshifts (e.g. Bertola et al. 2020; Gupta et al. 2022; Maiolino et al. 2024b). However, for the rest-frame $\gtrsim 20$ keV continuum of J1429 to have increased by a factor of > 2 would require an enormous change in column density on the order of $\Delta N_{\text{H}} \gtrsim 10^{24}$ cm⁻² (see Figure 1 of Boorman et al. 2025). Such extreme changes of Compton-thick column densities have been observed in the local universe (e.g., Risaliti et al. 2005; Marinucci et al. 2016; Marchesi et al. 2022), as well as rapid changes in obscuration on the order of weeks (e.g., Risaliti et al. 2002; Elvis et al. 2004; Torres-Albà et al. 2023); nevertheless, occurrences of both are drastically rarer (e.g., Ricci & Trakhtenbrot 2023). Lastly, for typical Compton-thick column densities, the true intrinsic unobscured rest-frame 2 – 10 keV luminosity would be $\sim 1.5\text{--}3$ orders of magnitude higher, which would be remarkably high.

5.2.2. Blazar

An alternative explanation for many of the properties of J1429+5447, including the rapid variability presented here, is that J1429+5447 is a blazar—that is, that we are seeing it along the jet axis. This interpretation would resolve tensions in many of the source’s properties, chief of which would be the extreme luminosity, as blazars are widely observed to be X-ray luminous, especially at high redshifts (Ighina et al. 2019). Additionally, Frey et al. (2011) note that J1429+5447 hosts a jet that is only 100 pc long in projection, despite the AGN being luminous and radio-loud; if seen face-on, however, the small size of this jet would merely be a projection effect (Xie et al. 2024). Blazar variability is observed to be bursty (e.g., Escudero Pedrosa et al. 2024), in keeping with

our observed dramatic brightening over a short time period despite otherwise consistent flux (Figure 5), and the compressed observational timescale of events seen along the jet (e.g., Singh & Meintjes 2020) means that the emission region could be larger than assumed for the un-beamed case.

However, other observed properties of J1419+5447 are not consistent with blazars, such that Medvedev et al. (2020) previously rejected that hypothesis. As discussed above, the VLASS radio flux densities are relatively consistent between epochs, as are other radio intensity measurements (see Table 1 in Medvedev et al. 2020). Similarly, the spectral slope of the radio emission is $\alpha \approx -0.7$ to -1.0 (Frey et al. 2011; Coppejans et al. 2017), classified as a steep-spectrum source, while blazars have typical values of $\alpha > -0.5$ (e.g., d’Antonio et al. 2019). Ighina et al. (2019) proposed a classification diagram for potential high-redshift blazars, requiring $\Gamma \lesssim 1.8$ and UV-to-X-ray slope⁵ $\tilde{\alpha}_{\text{OX}} < 1.355$; although J1429+5447 matches the latter ($\tilde{\alpha}_{\text{OX}} = 0.96_{-0.07}^{+0.11}$, Medvedev et al. 2020), the steep X-ray slope seen in all analyses so far is inconsistent with this expectation.

Of course, the properties of blazars are not always so easily confined, particularly at high redshift; indeed, multiple works now have reported that sources classified as blazars at high-redshift ($z > 4$) display contradictory qualities (i.e. classified as blazars with X-rays, but displaying misaligned/bent jets in radio; Sbarrato et al. 2015, 2021, 2022; Cao et al. 2017; Caccianiga et al. 2019; Ighina et al. 2019). Moreover, some $z > 5$ blazars detected in X-rays display softer photon indices ($\Gamma > 2$; An & Romani 2018, 2020) which has been interpreted as the peak of the synchrotron self-Compton component emerging at these energies. Furthermore, under the assumption J1429+5447 may be a progenitor for one of the powerful MeV blazars observed at lower redshifts, the average MeV blazar SED shape derived from Marcotulli et al. (2022) implies a rest-frame peak of a $L_{\text{X}} \sim 10^{46}$ erg s⁻¹ source at $E_b \sim 4$ MeV and an average photon index of $\Gamma_{\text{X}} = 1.70 \pm 0.14$, which is compatible to our derived NuSTAR and Chandra photon indices within a 90% significance level (see Figure 3). Even more compelling for our case, Khusanova et al. (2022) found that the radio spectrum of J1429+5447 is flat ($\alpha \sim -0.5$) below 1.4 GHz and shows similar properties (including lack of radio variability) to the $z = 6.10$ blazar source J0309+2717 (Belladitta et al. 2020; Ighina et al. 2022).

Given NOEMA observations showing evidence for significant jet impact on the quasar host’s gas (Li et al. 2024), it could be possible that the jet is being bent outside of the innermost accretion regions. As one potential manifestation of bending on our understanding of this source, if the face-on

⁵ $\tilde{\alpha}_{\text{OX}} = -0.3026 \log(L_{10 \text{ keV}}/L_{2500 \text{ \AA}})$

nature of the jet only emerges well away from the central engine, the much weaker magnetic fields may not produce the expected radio signatures of a typical blazar.

In the case that the X-ray jet is pointed at us, beaming would shorten the observed variability timescale (e.g., [Singh & Meintjes 2020](#)) by

$$t_{\text{rest}} = t_{\text{obs}} \times \delta / (1 + z), \quad (3)$$

where the Doppler factor (δ) is

$$\delta = (\Gamma_b(1 - \beta \cos \theta_V))^{-1} \quad (4)$$

for viewing angle θ_V , emission region speed β , and bulk Lorentz factor Γ_b . For a typical value of $\Gamma_b \sim 5 - 10$ (e.g. [Marcotulli et al. 2020](#); [Sbarrato et al. 2021](#)) in the limit of $\theta_V \rightarrow 0$, $t_{\text{source}} = t_{\text{obs}} \times \Gamma / (1 + z) \sim 2.7 - 5.5$ months. Using the same formalism as above, this would imply that the size of the X-ray emission region is larger: $R = 390 - 796 R_{\text{Schw}}$ ($0.07 - 0.1$ pc), placing it within the scale of the BLR region.

For a blazar jet, there are multiple ways that short-term multiwavelength variability could be produced, including a shock (e.g. [Baring et al. 2017](#)), magnetic reconnection (e.g. [Zhang et al. 2022](#)), or an increase or modification of the photon field surrounding the jet (see [Blandford et al. 2019](#); [Böttcher 2019](#); [Hovatta & Lindfors 2019](#), and references therein for recent reviews on the topic). The photon field could also be modified by a perturbation in the accretion disk (e.g. [Stern et al. 2018](#)) that propagates in the BLR clouds, or perhaps by a passage of a cloud in front of the jet, thereby acting as a mirror to enhance the radiation field (e.g. [Ghisellini & Madau 1996](#); [León-Tavares et al. 2013](#); [Chavushyan et al. 2020](#)).

A blazar interpretation for J1429+5447 would be exciting, as the detection of one blazar implies that a larger population of radio-loud AGN with similar properties—but not favorably aligned to our line of sight—exist at a similar redshift (e.g., [Belladitta et al. 2020](#)). Indeed, recent work has started to show evidence that a significant fraction of AGN in the early Universe are jetted (e.g., [Sbarrato et al. 2022](#); ?), such that the large number of known quasars should, in turn, imply a larger population of jetted quasars than currently seen. From the recent luminosity function work of [Marcotulli et al. \(2022\)](#), in the redshift bin $z = [6.0, 6.3]$ and within the highest luminosity range $L_{14-195 \text{ keV}} = [10^{47} - 10^{48}] \text{ erg s}^{-1}$, we would expect $N \lesssim 10$ blazars in an all-sky sample. Although this number can be thought of as an upper limit, being an extrapolation of the X-ray luminosity function, it is not improbable that radio-loud, X-ray luminous J1429+5447 is indeed one of the expected blazars at those redshifts.

5.2.3. Jets

Between the AGN and blazar interpretations is one in which the X-ray luminosity is being powered by jets. In particular, [Medvedev et al. \(2021\)](#) advanced this hypothesis, as did [Migliori et al. \(2023\)](#), based on the possible presence of a second or extended component. The fundamental concept of this emission is that the energy density of the CMB, which scales as $(1 + z)^4$, dominates over magnetic fields in these jets, and so most of their emission is in inverse Compton up-scattered X-rays instead of radio (e.g., [Ghisellini et al. 2014](#)). Direct evidence for this IC/CMB emission around $z \gtrsim 6$ quasars has recently been seen ([Connor et al. 2021b](#); [Ighina et al. 2022](#)), and for J1429+5447 the presence of large jets visible only in X-rays would rectify the shortness of the observed radio structures with the independent NOEMA arguments for active, powerful jets.

However, the rapid variability seen here contradicts this interpretation. The size of the X-ray producing regions of jets are significantly larger than the sub-pc-scale region permitted by the observed variation. [Migliori et al. \(2023\)](#) already constrained the location of the bulk of the X-ray emission to be at < 3 kpc and emphasized that, to explain the level of J1429+5447's X-ray luminosity, Doppler boosting would still be required in an IC/CMB jet scenario. For the significant originally observed luminosity of J1429+5447 to be due to non-beamed X-ray IC/CMB emission and for the observed short-term excess to be produced by a different mechanism, then the scale of the variation would have to be even more extreme. As such, the results of this work imply that the brightness of J1429+5447 is not due to extended, unbeamed emission from its jets.

5.2.4. Interloper Contamination

We must also consider the least exciting option, namely that the observed increase in flux came from one of the two interloper sources. In this case, J1429+5447 did not vary in flux, but, instead, either I-NE or I-SW (or both) increased by a factor of 10 in brightness in around 50 days in their rest frames; the *NuSTAR* image, with its worse angular resolution, masked the origin of the increase in flux. This scenario is excluded by design in our modeling, due to the following reasons.

1. One decade in flux in such a short time scale would be a massive outlier in typical AGN variability (compare to Figure 4 and see Appendix C), even more so than the already impressive value assumed in this work. Yet, unlike J1429+5447, the two interloper sources are not otherwise typical of sources that would produce such extreme flux variations; neither have associated radio sources, nor do they have X-ray spectra typical of blazars. Moreover, unlike J1429+5447, these sources are not already outliers in X-ray emission. As such,

we would not expect them to produce such a massive outburst.

2. Although the *NuSTAR* observation suffers from relatively poor angular resolution, and so the source is smeared over the position of the quasar and interlopers, the centroid of the source nevertheless aligns with that of J1429+5447 (Figure 1). *NuSTAR* has an astrometric accuracy of roughly 8'' to 90% (Harrison et al. 2013), and so offsets of 30'' (I-NE) or 45'' (I-SW) would be significant outliers. Conversely, there is an unrelated X-ray source, J142922.1+544428, seen at the edge of the *NuSTAR* detectors located at roughly the expected astrometric precision.

5.3. Future Outlook

For J1429+5447—as well as for many other quasars in the $z \gtrsim 6$ epoch—both multiwavelength and coordinated observations are necessary to understand the nature of the source (e.g., Bañados et al. 2024a,b). Based on the variability seen here, the radio properties, which are key to determining the possibility of the source being a blazar, need to be coordinated to guard against flux variation inducing an incorrect measurement of the spectral shape, while simultaneity with X-ray observations is critical to assess jet conditions. Likewise, IR imaging and spectroscopy, and sub-mm imaging can constrain the stellar and SMBH parameters, providing the needed context of the host galaxy, its merger environment, and how physically impactful the jets are.

Given the significant exposure time required to detect J1429+5447 with *NuSTAR*, and given that J1429+5447 is, even with variability, the most X-ray luminous $z \gtrsim 6$ quasar, it is likely that this will be the most distant object ever robustly detected by the observatory. Nevertheless, it is an indication of what will be possible with a future, more sophisticated hard X-ray telescope such as the proposed probe-class *High Energy X-ray Probe (HEX-P)*; Madsen et al. 2024). Although *HEX-P* was not selected in the 2023 Astrophysics Probe Explorer opportunity, the challenges that motivate it still remain. The broadband X-ray coverage (0.2–80 keV) proposed for *HEX-P* would enable simultaneous soft-to-hard measurements, constraining the broadband high-energy spectrum to levels beyond current capabilities (at both soft and hard energies)—in significantly shorter exposure times. Moreover, the high sensitivity and low background at high energies would allow us to not only detect countless more $z \gtrsim 6$ quasars beyond 5 keV but to fit more complex and informative models to this population, such as first measurements of their coronal breaks. The full capabilities of *HEX-P* on blazar and AGN science were explored in detail by Marcotulli et al. (2024), Boorman et al. (2024), Kammoun et al. (2024) and Pfeifle et al. (2024), but this pathfinder observation with *NuSTAR* demonstrates that high-redshift science

can be an important part of the next *HEX-P* caliber mission’s capabilities.

6. SUMMARY

In this work, we have presented *NuSTAR* observations of J1429+5447, a $z = 6.19$ radio-loud quasar that is the most X-ray luminous quasar currently known in the early universe. These observations establish a new record for the most distant object observed by *NuSTAR* (surpassing blazars B2 1023+25 at $z = 5.3$ and QSO J0906+6930 at $z = 5.48$; Sbarrato et al. 2013; An & Romani 2018) and demonstrate the capabilities of observing hard-energy X-rays into the Epoch of Reionization.

Owing to an unrelated *Chandra* observation four months prior, we were able to fit the quasar’s X-ray spectrum while self-consistently accounting for contamination from two nearby sources. We found that, over just two weeks in the quasar rest-frame between the *Chandra* and *NuSTAR* observations, the flux of the source increased by 0.4 dex.

This observed X-ray variability is one of the most extreme seen at these redshifts, and it is potentially indicative of significant events in either the quasar accretion region or the jet. Further observations, some of which are already underway, are needed to further establish the nature of these fluctuations.

We thank the journal anonymous referee for the constructive review. Support for this work was provided by the National Aeronautics and Space Administration through Chandra Award Number GO3-24069X, GO8-19093X, and GO0-21101X issued by the *Chandra* X-ray Center, which is operated by the Smithsonian Astrophysical Observatory for and on behalf of the National Aeronautics Space Administration under contract NAS8-03060.

This research has made use of data from the *NuSTAR* mission, a project led by the California Institute of Technology, managed by the Jet Propulsion Laboratory, and funded by the National Aeronautics and Space Administration. Data analysis was performed using the *NuSTAR* Data Analysis Software (NuSTARDAS), jointly developed by the ASI Science Data Center (SSDC, Italy) and the California Institute of Technology (USA). The scientific results reported in this article are based on observations made by the *Chandra X-ray Observatory* contained in CDC 308. This research has made use of software provided by the *Chandra* X-ray Center (CXC) in the application package CIAO.

LM acknowledges that support for this work was provided by NASA through the NASA Hubble Fellowship grant No. HST-HF2-51486.001-A awarded by the Space Telescope Science Institute, which is operated by the Association of Universities for Research in Astronomy, Inc., for NASA, under contract NAS5-26555. T.C. and A.S. acknowledge support from NASA Contract NAS8-03060 to the Chandra X-ray Center. Portions of T.C.’s research were supported by an appointment to the NASA Postdoctoral Program at the Jet Propulsion Laboratory, California Institute of Technology, administered by Universities Space Research Association under contract with NASA. The National Radio Astronomy Observatory is a facility of the National Science Foundation operated under coopera-

tive agreement by Associated Universities, Inc. G.M. acknowledges financial support from the INAF mini-grant “The high-energy view of jets and transients” (Bando Ricerca Fondamentale INAF 2022). CM acknowledges support from ANID BASAL project FB210003. YK thanks the support of the German Space Agency (DLR) through

the program LEGACY 50OR2303. Research at the Naval Research Laboratory is supported by NASA DPR S-15633-Y.

Facilities: NuSTAR, CXO

Software: BXA (Buchner et al. 2014), CIAO (Fruscione et al. 2006), PyFITS (Barrett & Bridgman 1999), XSPEC (Arnaud 1996)

APPENDIX

A. CROSS-CALIBRATION TEST

An important factor to take into account in our analysis is the effect of cross-calibration constants between different instruments. Specifically, Madsen et al. (2017, cf. Table 6 in their work) showed that for a simultaneous *NuSTAR/Chandra* observation of a non-variable soft power-law spectrum ($\Gamma \sim 2.5$) source, if the constants of FPMA/B are frozen to 1, then the constants assigned to the *Chandra* ACIS spectra should be 1.09/1.10. In other words, due to calibration systematics, the *Chandra*-derived flux is systematically $\sim 10\%$ higher than the *NuSTAR* one.

To test whether this factor would make any difference to our analysis, we repeated the fit detailed in Section 4.3 assigning (and freezing) the value of 1.09 to the cross-calibration constant of the three *Chandra* spectra (J1429+5447, I-NE, I-SW), while keeping the cross-calibration constant of the co-added FPMAs frozen to unity. The results show that making this assumption of systematics in the cross-calibration returns an even stronger variability of J1429+5447. This finding, combined with the fact that the most updated *NuSTAR* calibration files have been re-calibrated so that the derived *NuSTAR* flux is 5-15% higher⁶ (hence should be comparable to the *Chandra* flux, see Madsen et al. 2022), validates not just keeping the cross-normalization frozen to unity for all instruments, but also that this choice ultimately does not impact our findings (see also discussion in Sec. 5.3 of Sobolewska et al. 2023).

B. HIGH-ENERGY CUTOFF AND BROKEN POWER LAW SCENARIOS

In our analysis, we conclude that the observed spectrum of J1429+5447 is well explained by a power law. However, we also tested more complex—yet physically motivated—shapes to test if J1429+5447 shows a break or curvature in the spectrum (see Section 4.4 for details on the fitting procedure). We use both a power-law with exponential cut-off (M4) and a broken power-law (M3) to interpret the data. The power law with exponential cutoff gives us an upper limit on the cut-off energy value of $E_{\text{cut-off, rest-frame}} > 169 \text{ keV}$ and $\Gamma = 2.15^{+0.24}_{-0.19}$. The broken power law gives us $\Gamma_1 = 2.34^{+0.26}_{-0.27}$, $\Gamma_2 = 2.21^{+0.37}_{-2.14}$ and $\log(E_{\text{break, rest-frame}}, \text{keV}) = 1.88^{+0.93}_{-0.16}$. Within uncertainties, all the scenarios are consistent with the simple power-law case. In Figure 6 we showcase the spectral posterior distribution of these two models in the 3–78 keV band. It can be seen that in either case, a broken/cutoff spectrum is fully consistent (within the 68% percentile range) with the power-law scenario.

C. INTERLOPERS POSTERIOR FLUX AND PHOTON INDEX DISTRIBUTION

The combined fit detailed in Section 4.3 returns the posterior probability on all fitted parameters and flux distributions for all the loaded spectra. For completeness, we show in Figure 7 the version of Figure 3 including the interlopers. This Figure highlights how subdominant the interlopers are with respect to J1429+5447. As noted in Section 5.2.4, the interlopers would have needed to vary approximately by a decade in brightness in around 50 days rest-frame to recover the *NuSTAR* flux reported in this work.

REFERENCES

- Ai, Y., Dou, L., Fan, X., et al. 2016, *ApJL*, 823, L37
- Akylas, A., & Georgantopoulos, I. 2021, *A&A*, 655, A60
- An, H., & Romani, R. W. 2018, *ApJ*, 856, 105
- An, H., & Romani, R. W. 2020, *ApJ*, 904, 27
- Arnaud, K. A. 1996, *adass V*, 101, 17
- Bañados, E., Venemans, B. P., Morganson, E., et al. 2015, *ApJ*, 804, 118
- Bañados, E., Venemans, B. P., Decarli, R., et al. 2016, *ApJS*, 227, 11
- ⁶ See Calibration page entry 2021-10-26: https://nustarsoc.caltech.edu/NuSTAR_Public/NuSTAROperationSite/software_calibration.php

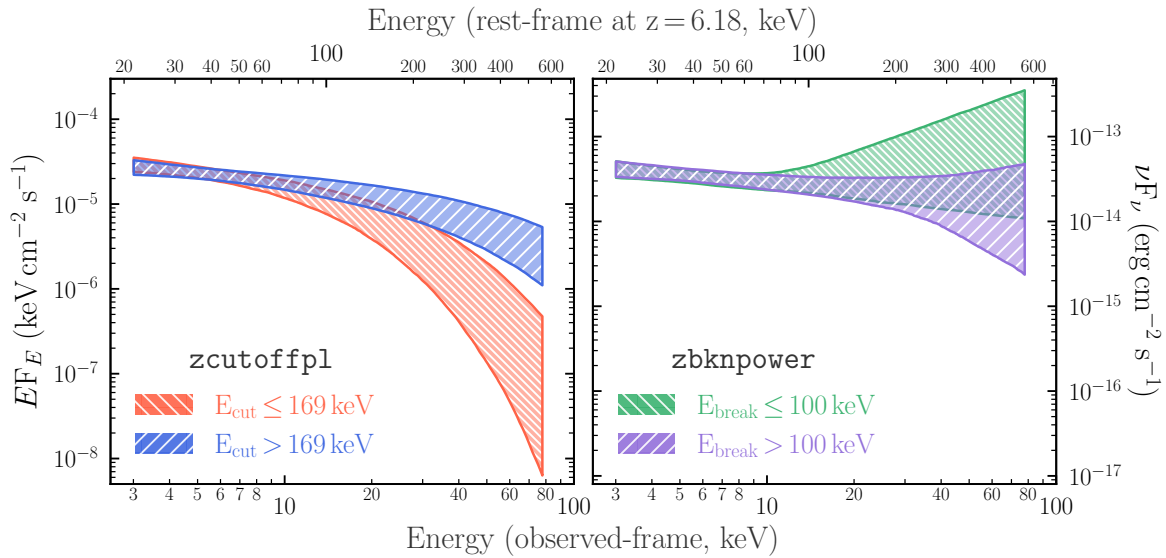


Figure 6. 3 – 78 keV spectrum of J1429+5447 using a more complex spectral model. **Left:** redshifted power law with high-energy cutoff. The shaded bands in the plot represent the 68th percentile range regions of model predictions as calculated considering all posteriors for which $E_{\text{cut,rest-frame}} < 169$ keV (orange, backward-slashed shaded region) and $E_{\text{cut,rest-frame}} > 169$ keV (blue, forward-slashed shaded region, i.e. akin to the simple power-law model). **Right:** redshifted broken power law. The shaded bands in the plot represent the 68th percentile range regions of model predictions as calculated considering all posteriors for which $E_{\text{b,rest-frame}} \leq 100$ keV (green, backward-slashed shaded region, i.e. region of the posterior that includes values of E_{b} at 68% HDI level from the mode of the distribution) and $E_{\text{b,rest-frame}} > 100$ keV (purple, forward-slashed shaded region, i.e. akin to the simple power-law model). These plots show that, within uncertainties, we cannot determine whether a complex modeling of the source is favored. Therefore, the best-fit representation of the data at hand is the simplest one.

Bañados, E., Venemans, B. P., Mazzucchelli, C., et al. 2018a, *Nature*, 553, 473

Bañados, E., Connor, T., Stern, D., et al. 2018b, *ApJL*, 856, L25

Bañados, E., Schindler, J.-T., Venemans, B. P., et al. 2023, *ApJS*, 265, 29

Bañados, E., Momjian, E., Connor, T., et al. 2024a, *Nature Astronomy*

Bañados, E., Khusanova, Y., Decarli, R., et al. 2024b, *ApJL*, 977, L46

Baloković, M., Harrison, F. A., Madejski, G., et al. 2020, *ApJ*, 905, 41

Baring, M. G., Böttcher, M., & Summerlin, E. J. 2017, *MNRAS*, 464, 4875

Barrett, P. E., & Bridgman, W. T. 1999, *adass VIII*, 172, 483

Belladitta, S., Moretti, A., Caccianiga, A., et al. 2020, *A&A*, 635, L7

Bertola, E., Dadina, M., Cappi, M., et al. 2020, *A&A*, 638, A136

Blandford, R., Meier, D., & Readhead, A. 2019, *ARA&A*, 57, 467

Boorman, P. G., Torres-Albà, N., Annuar, A., et al. 2024, *Frontiers in Astronomy and Space Sciences*, 11, 1335459

Boorman, P. G., Gandhi, P., Buchner, J., et al. 2025, *ApJ*, 978, 118

Böttcher, M. 2019, *Galaxies*, 7, 20

Brightman, M., Silverman, J. D., Mainieri, V., et al. 2013, *MNRAS*, 433, 2485

Bromm, V., Coppi, P. S., & Larson, R. B. 1999, *ApJL*, 527, L5

Buchner, J. 2016, *Astrophysics Source Code Library*, ascl:1610.011

Buchner, J. 2021, *The Journal of Open Source Software*, 6, 3001

Buchner, J. 2023, *Statistics Surveys*, 17, 169

Buchner, J., & Boorman, P. 2023, *arXiv e-prints*, arXiv:2309.05705

Buchner, J., Georgakakis, A., Nandra, K., et al. 2014, *A&A*, 564, A125

Caccianiga, A., Moretti, A., Belladitta, S., et al. 2019, *MNRAS*, 484, 204

Cao, H. M., Frey, S., Gabányi, K. É., et al. 2017, *MNRAS*, 467, 950

Carnerero, M. I., Raiteri, C. M., Villata, M., et al. 2017, *MNRAS*, 472, 3789

Cash, W. 1979, *ApJ*, 228, 939

Chavushyan, V., Patiño-Álvarez, V. M., Amaya-Almazán, R. A., & Carrasco, L. 2020, *ApJ*, 891, 68

Connor, T., Bañados, E., Cappelluti, N., & Foord, A. 2024, *Universe*, 10, 227

Connor, T., Stern, D., Bañados, E., & Mazzucchelli, C. 2021a, *ApJL*, 922, L24

Connor, T., Bañados, E., Stern, D., et al. 2019, *ApJ*, 887, 171

Connor, T., Bañados, E., Mazzucchelli, C., et al. 2020, *ApJ*, 900, 189

Connor, T., Bañados, E., Stern, D., et al. 2021b, *ApJ*, 911, 120

Coppejans, R., van Velzen, S., Intema, H. T., et al. 2017, *MNRAS*, 467, 2039

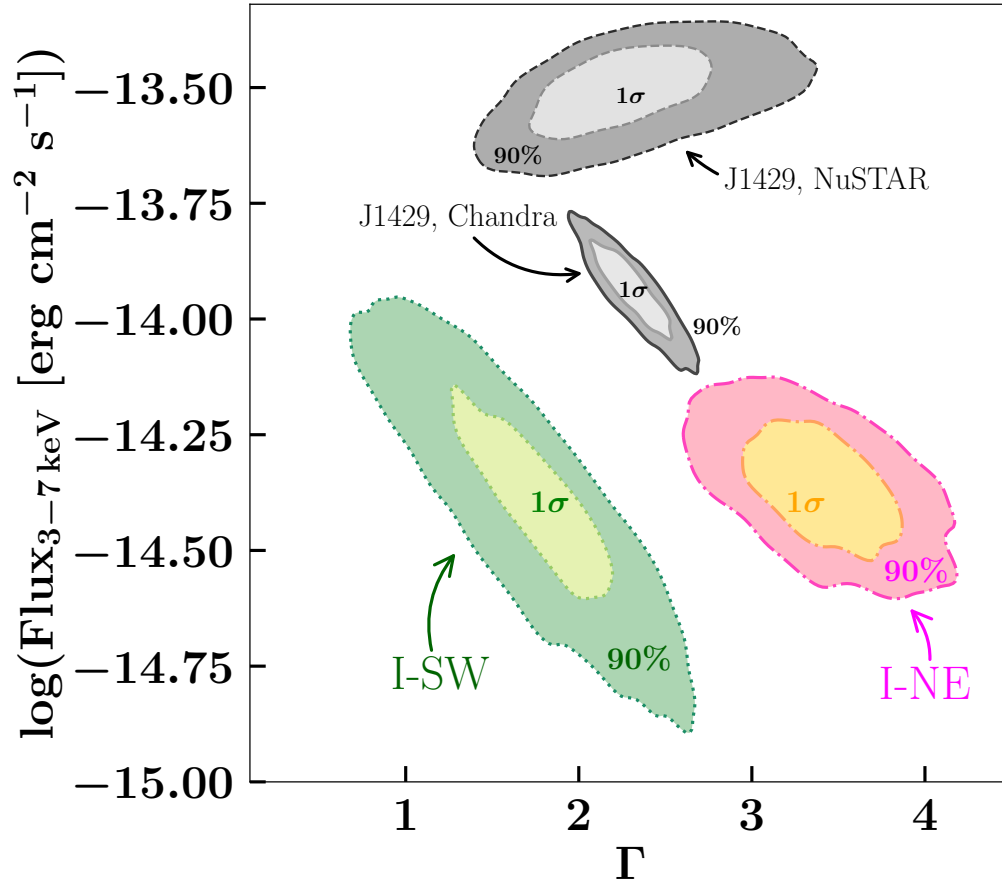


Figure 7. 3 – 7 keV posterior flux distribution versus the full-band photon index posterior distribution for J1429+5447 (*Chandra* epoch: solid lines; *NuSTAR* epoch: dashed lines), I-NE (dotted lines) and I-SW (dash-dotted lines) obtained with the simultaneous fit of the 3 *Chandra* sources and the co-added FPMAs (details in Section 4.3). The 1σ and 90% contour levels are reported in the plot. This is an extension of Figure 3 to show how subdominant I-NE and I-SW are in the 3 – 7 keV band compared to J1429+5447.

Coppi, P. S. 1999, in *Astronomical Society of the Pacific Conference Series*, Vol. 161, *High Energy Processes in Accreting Black Holes*, ed. J. Poutanen & R. Svensson, 375

Cuillandre, J.-C. J., Withington, K., Hudelot, P., et al. 2012, *Proc. SPIE*, 8448, 84480M

d’Antonio, D., Giroletti, M., Giovannini, G., & Maini, A. 2019, *MNRAS*, 490, 5798

Duncan, K. J. 2022, *MNRAS*, 512, 3662

Elvis, M., Risaliti, G., Nicastro, F., et al. 2004, *ApJL*, 615, L25

Escudero Pedrosa, J., Agudo, I., Tramacere, A., et al. 2024, *A&A*, 682, A100

Fabian, A. C., Lohfink, A., Kara, E., et al. 2015, *MNRAS*, 451, 4375

Fan, X., Bañados, E., & Simcoe, R. A. 2023, *ARA&A*, 61, 373

Farina, E. P., Schindler, J.-T., Walter, F., et al. 2022, *ApJ*, 941, 106

Frey, S., Paragi, Z., Gurvits, L. I., Gabányi, K. É., & Cseh, D. 2011, *A&A*, 531, L5

Fruscione, A., McDowell, J. C., Allen, G. E., et al. 2006, *Proc. SPIE*, 6270, 62701V

Garmire, G. P., Bautz, M. W., Ford, P. G., Nousek, J. A., & Ricker, George R., J. 2003, *Proc. SPIE*, 4851, 28

Georgakakis, A., Buchner, J., Ruiz, A., et al. 2024, *MNRAS*, 531, 4524

Ghisellini, G., Celotti, A., Tavecchio, F., Haardt, F., & Sbarrato, T. 2014, *MNRAS*, 438, 2694

Ghisellini, G., Haardt, F., Ciardi, B., et al. 2015, *MNRAS*, 452, 3457

Ghisellini, G., & Madau, P. 1996, *MNRAS*, 280, 67

Gokus, A., Böttcher, M., Errando, M., et al. 2024, *ApJ*, 974, 38

Gordon, C., & Arnaud, K. 2021, *Astrophysics Source Code Library*, ascl:2101.014

Greenwell, C. L., Klindt, L., Lansbury, G. B., et al. 2024, *ApJS*, 273, 20

Gupta, N., Srianand, R., Momjian, E., et al. 2022, *ApJL*, 927, L24

Haardt, F., & Maraschi, L. 1991, *ApJL*, 380, L51

Habouzit, M., Volonteri, M., Latif, M., Dubois, Y., & Peirani, S. 2016, *MNRAS*, 463, 529

Harrison, F. A., Craig, W. W., Christensen, F. E., et al. 2013, *ApJ*, 770, 103

- HI4PI Collaboration, Ben Bekhti, N., Flöer, L., et al. 2016, *A&A*, 594, A116
- Hovatta, T., & Lindfors, E. 2019, *NewAR*, 87, 101541
- Ighina, L., Caccianiga, A., Moretti, A., et al. 2019, *MNRAS*, 489, 2732
- Ighina, L., Moretti, A., Tavecchio, F., et al. 2022, *A&A*, 659, A93
- Jolley, E. J. D., & Kuncic, Z. 2008, *MNRAS*, 386, 989
- Kaastra, J. S., & Bleeker, J. A. M. 2016, *A&A*, 587, A151
- Kammoun, E., Lohfink, A. M., Masterson, M., et al. 2024, *Frontiers in Astronomy and Space Sciences*, 10, 1308056
- Kellermann, K. I., Sramek, R., Schmidt, M., Shaffer, D. B., & Green, R. 1989, *AJ*, 98, 1195
- Khusanova, Y., Bañados, E., Mazzucchelli, C., et al. 2022, *A&A*, 664, A39
- Lacy, M., Baum, S. A., Chandler, C. J., et al. 2020, *PASP*, 132, 035001
- Lanzuisi, G., Gilli, R., Cappi, M., et al. 2019, *ApJL*, 875, L20
- Larson, R. L., Finkelstein, S. L., Kocevski, D. D., et al. 2023, *ApJL*, 953, L29
- León-Tavares, J., Chavushyan, V., Patiño-Álvarez, V., et al. 2013, *ApJL*, 763, L36
- Lewis, G. F., & Brewer, B. J. 2023, *Nature Astronomy*, 7, 1265
- Li, J., Wang, R., Pensabene, A., et al. 2024, *ApJ*, 962, 119
- Li, J.-T., Wang, F., Yang, J., et al. 2021, *MNRAS*, 504, 2767
- Lodato, G., & Natarajan, P. 2006, *MNRAS*, 371, 1813
- Luo, Y., Shlosman, I., Nagamine, K., & Fang, T. 2020, *MNRAS*, 492, 4917
- Lusso, E., & Risaliti, G. 2016, *ApJ*, 819, 154
- Madsen, K. K., Beardmore, A. P., Forster, K., et al. 2017, *AJ*, 153, 2
- Madsen, K. K., Forster, K., Grefenstette, B., Harrison, F. A., & Miyasaka, H. 2022, *Journal of Astronomical Telescopes, Instruments, and Systems*, 8, 034003
- Madsen, K. K., García, J. A., Stern, D., et al. 2024, *Frontiers in Astronomy and Space Sciences*, 11, 1357834
- Maiolino, R., Scholtz, J., Witstok, J., et al. 2024a, *Nature*, 627, 59
- Maiolino, R., Risaliti, G., Signorini, M., et al. 2024b, *arXiv e-prints*, arXiv:2405.00504
- Marchesi, S., Zhao, X., Torres-Albà, N., et al. 2022, *ApJ*, 935, 114
- Marcotulli, L., Paliya, V., Ajello, M., et al. 2020, *ApJ*, 889, 164
- Marcotulli, L., Ajello, M., Urry, C. M., et al. 2022, *ApJ*, 940, 77
- Marcotulli, L., Ajello, M., Böttcher, M., et al. 2024, *Frontiers in Astronomy and Space Sciences*, 11, 1290057
- Marinucci, A., Bianchi, S., Matt, G., et al. 2016, *MNRAS*, 456, L94
- Matsuoka, Y., Iwasawa, K., Onoue, M., et al. 2022, *ApJS*, 259, 18
- Medvedev, P., Gilfanov, M., Sazonov, S., Schartel, N., & Sunyaev, R. 2021, *MNRAS*, 504, 576
- Medvedev, P., Sazonov, S., Gilfanov, M., et al. 2020, *MNRAS*, 497, 1842
- Migliori, G., Siemiginowska, A., Sobolewska, M., et al. 2023, *MNRAS*, 524, 1087
- Mingo, B., Croston, J. H., Hardcastle, M. J., et al. 2019, *MNRAS*, 488, 2701
- Molina, M., Malizia, A., Bassani, L., et al. 2019, *MNRAS*, 484, 2735
- Moretti, A., Ghisellini, G., Caccianiga, A., et al. 2021, *ApJ*, 920, 15
- Nanni, R., Vignali, C., Gilli, R., Moretti, A., & Brandt, W. N. 2017, *A&A*, 603, A128
- Nanni, R., Gilli, R., Vignali, C., et al. 2018, *A&A*, 614, A121
- Ochsenbein, F., Bauer, P., & Marcout, J. 2000, *A&AS*, 143, 23
- Onoue, M., Bañados, E., Mazzucchelli, C., et al. 2020, *ApJ*, 898, 105
- Pacucci, F., Nguyen, B., Carniani, S., Maiolino, R., & Fan, X. 2023, *ApJL*, 957, L3
- Pfeifle, R. W., Boorman, P. G., Weaver, K. A., et al. 2024, *Frontiers in Astronomy and Space Sciences*, 11, 1304652
- Ponti, G., Papadakis, I., Bianchi, S., et al. 2012, *A&A*, 542, A83
- Puccetti, S., Comastri, A., Fiore, F., et al. 2014, *ApJ*, 793, 26
- Ricci, C., & Trakhtenbrot, B. 2023, *Nature Astronomy*, 7, 1282
- Ricci, C., Trakhtenbrot, B., Koss, M. J., et al. 2017, *ApJS*, 233, 17
- Ricci, C., Ho, L. C., Fabian, A. C., et al. 2018, *MNRAS*, 480, 1819
- Risaliti, G., Elvis, M., Fabbiano, G., Baldi, A., & Zezas, A. 2005, *ApJL*, 623, L93
- Risaliti, G., Elvis, M., & Nicastro, F. 2002, *ApJ*, 571, 234
- Sbarrato, T., Ghisellini, G., Giovannini, G., & Giroletti, M. 2021, *A&A*, 655, A95
- Sbarrato, T., Ghisellini, G., Tagliaferri, G., et al. 2015, *MNRAS*, 446, 2483
- Sbarrato, T., Ghisellini, G., Tagliaferri, G., et al. 2022, *A&A*, 663, A147
- Sbarrato, T., Tagliaferri, G., Ghisellini, G., et al. 2013, *ApJ*, 777, 147
- Serafinelli, R., De Rosa, A., Tortosa, A., et al. 2024, *A&A*, 690, A145
- Shen, Y., Richards, G. T., Strauss, M. A., et al. 2011, *ApJS*, 194, 45
- Shen, Y., Wu, J., Jiang, L., et al. 2019, *ApJ*, 873, 35
- Singh, K. K., & Meintjes, P. J. 2020, *Astronomische Nachrichten*, 341, 713
- Sobolewska, M., Siemiginowska, A., Migliori, G., et al. 2023, *ApJ*, 948, 81
- Stern, D., McKernan, B., Graham, M. J., et al. 2018, *ApJ*, 864, 27
- Suh, H., Hasinger, G., Steinhardt, C., Silverman, J. D., & Schramm, M. 2015, *ApJ*, 815, 129
- Timlin, John D., I., Brandt, W. N., Zhu, S., et al. 2020, *MNRAS*, 498, 4033
- Torres-Albà, N., Marchesi, S., Zhao, X., et al. 2023, *A&A*, 678, A154
- Torres-Albà, N., Marchesi, S., Zhao, X., et al. 2021, *ApJ*, 922, 252
- Tortosa, A., Ricci, C., Arévalo, P., et al. 2023, *MNRAS*, 526, 1687

- Trakhtenbrot, B., Ricci, C., Koss, M. J., et al. 2017, *MNRAS*, 470, 800
- Urry, C. M., & Padovani, P. 1995, *PASP*, 107, 803
- Vito, F., Brandt, W. N., Bauer, F. E., et al. 2019a, *A&A*, 628, L6
- Vito, F., Brandt, W. N., Bauer, F. E., et al. 2019b, *A&A*, 630, A118
- Vito, F., Mignoli, M., Gilli, R., et al. 2022, *A&A*, 663, A159
- Volonteri, M., Habouzit, M., & Colpi, M. 2021, *Nature Reviews Physics*, 3, 732
- Wachter, K., Leach, R., & Kellogg, E. 1979, *ApJ*, 230, 274
- Wang, F., Yang, J., Fan, X., et al. 2019, *ApJ*, 884, 30
- Wang, F., Yang, J., Fan, X., et al. 2021a, *ApJL*, 907, L1
- Wang, F., Fan, X., Yang, J., et al. 2021b, *ApJ*, 908, 53
- Whalen, D. J., & Fryer, C. L. 2012, *ApJL*, 756, L19
- Whitmore, B. C., Allam, S. S., Budavári, T., et al. 2016, *AJ*, 151, 134
- Wik, D. R., Hornstrup, A., Molendi, S., et al. 2014, *ApJ*, 792, 48
- Willott, C. J., Delorme, P., Reylé, C., et al. 2010, *AJ*, 139, 906
- Wilms, J., Allen, A., & McCray, R. 2000, *ApJ*, 542, 914
- Wise, J. H., Regan, J. A., O'Shea, B. W., et al. 2019, *Nature*, 566, 85
- Xie, Z.-L., Bañados, E., Belladitta, S., et al. 2024, *ApJ*, 964, 98
- Yang, J., Wang, F., Fan, X., et al. 2020, *ApJL*, 897, L14
- Yang, J., Fan, X., Wang, F., et al. 2022, *ApJL*, 924, L25
- Zappacosta, L., Piconcelli, E., Fiore, F., et al. 2023, *A&A*, 678, A201
- Zhang, H., Li, X., Giannios, D., et al. 2022, *ApJ*, 924, 90